International Journal of Plasticity 194 (2025) 104474



Contents lists available at ScienceDirect

International Journal of Plasticity

journal homepage: www.elsevier.com/locate/ijplas





Experimental analysis and modeling of anisotropic ductile damage in non-proportional extreme low-cycle biaxial loading with shear-tension histories

Zhichao Wei [a,b,*], Guoxi Mao [a], Steffen Gerke [b], Sebastian Münstermann [a], Michael Brünig [b]

[a] Institute of Metal Forming, RWTH Aachen University, Intzestr. 10, D-52072 Aachen, Germany
[b] Institute for Engineering Mechanics and Structural Analysis, University of the Bundeswehr Munich, Werner-Heisenberg-Weg 39, D-85577 Neubiberg, Germany

ARTICLE INFO

Keywords:
Material modeling
Extreme low-cycle experiments
Non-proportional loading
Ductile damage and fracture
Non-proportional hardening
Machine learning tool

ABSTRACT

This paper discusses the ductile damage and fracture behavior based on newly designed and performed non-proportional, non-reverse, extremely low-cycle experiments. In contrast to most extremely low-cycle experiments, which involve reverse loading histories or are restricted to a limited small plastic strain range, this study proposes novel non-proportional tension-to-shear (TS) and shear-to-tension (ST) loading patterns. Different combinations of displacement increments are applied within individual cyclic loading patterns, ensuring that specimen failure is governed by ductile damage and fracture under large plastic deformations. Numerical calculations are based on an advanced cyclic plastic-damage constitutive model with combined hardening laws. A novel non-proportionality parameter incorporating the effective back stress tensor is introduced into the combined hardening formulation to account for non-proportional hardening, allowing for a more accurate characterization of plastic behavior under non-proportional cyclic loading conditions. Digital image correlation (DIC) is used to analyze the global load–displacement curves and local strain fields, enabling comparison with the numerical results at both macroscopic and microscopic levels. Scanning electron microscope (SEM) and light optical microscope (LOM) images were taken from the fracture surfaces as well as both fractured and unfractured notch areas of the specimen, respectively. A novel quantitative analysis was introduced to evaluate the obtained SEM images using a convolutional neural network (CNN) approach, whereas LOM images were analyzed with the open-source software ImageJ. The present work highlights that non-proportional loading histories and shear-tension cyclic loading sequences with various plastic amplitudes significantly influence on the material's plastic and ductile damage behavior.

1. Introduction

With economic development and a growing emphasis on sustainability, the demand for efficient material usage is increasing. Thus, a more accurate understanding of material behavior becomes essential. Complex loading conditions often significantly impact the service life of engineering structures. For instance, offshore wind structures are frequently subjected to multiaxial non-proportional and cyclic loading due to varying and combined effects of wind and wave directions. Additionally, forming and rolling

* Corresponding author at: Institute of Metal Forming, RWTH Aachen University, Intzestr. 10, D-52072 Aachen, Germany.
E-mail addresses: zhichao.wei@ibf.rwth-aachen.de, zhichao.wei@unibw.de (Z. Wei).

https://doi.org/10.1016/j.ijplas.2025.104474
Received 4 July 2025; Received in revised form 6 September 2025
Available online 12 September 2025
0749-6419/© 2025 The Author(s). Published by Elsevier Ltd. This is an open access article under the CC BY-NC-ND license (http://creativecommons.org/licenses/by-nc-nd/4.0/).

processes in material manufacturing are subjected to cyclic loading conditions. To enhance material efficiency and optimize resource usage in various engineering structures, numerical prediction is one of the most effective and cost-efficient approaches. Since plastic deformations and damage are irreversible and significantly influence material behavior, such as reduction of elastic properties due to the initiation and evolution of damage, special focus should be placed on accurately predicting plasticity and damage evolution under different complex loading conditions.

The von Mises plasticity model (von Mises, 1913) is widely used in industry due to its simplicity and effectiveness in describing plastic behavior under various complex loading conditions. However, it neglects the influence of stress invariants, such as the different material responses in tension and compression, commonly referred to as the stress differential (SD) effect. Several stress-invariant-dependent plasticity models have been proposed in the literature (Spitzig et al., 1975; Li et al., 2016; Bai and Wierzbicki, 2008; Lou and Yoon, 2023; Voyiadjis et al., 2013; Yoon et al., 2014; Lou et al., 2020; Brünig et al., 2023). Among them, the Drucker–Prager (Drucker and Prager, 1952) model is one of the most simplified, incorporating the first stress invariant into the von Mises plasticity framework. Strain hardening is another key factor in characterizing plastic behavior after yielding. The isotropic hardening model describes the expansion of the yield surface, whereas the kinematic hardening model accounts for the translation of the yield surface in stress space. To accurately capture the strain hardening behavior, especially under cyclic loading conditions influenced by the Bauschinger effect, combined hardening models are widely used. Moreover, within the concept of combined hardening, Ohno (1982) proposed a non-hardening effect, where no isotropic hardening occurs within a specific region. Wei et al. (2023b) and Daroju et al. (2022) also observed and reported changes in the hardening ratio for different aluminum alloys subjected to various cyclic loading patterns. In addition, extra non-proportional strain hardening may occur due to the non-proportionality of the cyclic loading conditions (Lamba and Sidebottom, 1978; Jiang and Kurath, 1997; Shamsaei et al., 2010; Xing et al., 2019; Iftikhar and Khan, 2021; Hou et al., 2022). A large number of mathematical models have been proposed over the past three decades to predict kinematic hardening and non-proportional hardening (Frederick and Armstrong, 2007; Chaboche, 1986; Benallal and Marquis, 1987; Jiang and Kurath, 1997; Kang et al., 2005; Barlat et al., 2011; Ohno et al., 2021; Ning et al., 2025).

Furthermore, distortional hardening (Kurtyka and Życzkowski, 1996; François, 2001; Barlat et al., 2011; Shutov and Ihlemann, 2012; Iftikhar and Khan, 2021; Feigenbaum and Dafalias, 2007; Liu et al., 2011) is employed to characterize changes in the shape of the yield surface resulting from variations in the loading path, in contrast to conventional isotropic or kinematic hardening models. In François (2001), a distortional hardening model is developed by modifying the von Mises yield criterion, where the conventional deviatoric stress is substituted with a distorted stress formulation to capture the evolution of an egg-shaped yield surface. A decade ago, the HAH model proposed by Barlat et al. (2011) described the distortion of the yield surface through the introduction of anisotropic hardening based on homogeneous yield functions. More recently, hydrostatic pressure dependence has been incorporated into the distortional plasticity framework (Barlat et al., 2020). Shutov and Ihlemann (2012) employed second-rank backstress-like tensors to characterize the distortion of the yield surface under changes in the loading path.

The Gurson-type coupled damage models (Gurson, 1977; Tvergaard and Needleman, 1984) and continuum damage models (Kachanov, 1958; Lemaitre, 1985; Chaboche, 1988; Brünig, 2003; Abu Al-Rub and Voyiadjis, 2003; Balieu and Kringos, 2015; Badreddine and Saanouni, 2017) are extensively used in the numerical prediction of damage behavior. Gurson (1977) incorporated the void fraction into the yield function to model the softening behavior. Although the formulation of the proposed theories is simple, it cannot capture the degradation of the elastic properties caused by material damage. A similar concept was proposed by Lian et al. (2013), in which the damage evolution is based on energy dissipation. The continuum damage model was first proposed by Kachanov (1958) to simulate the progressive degradation of elastic properties. Owing to its efficiency, simplicity of parameter identification, reasonable predictive capability for large-scale computations, and low computational cost, it has been extensively developed in recent years. In addition, damage is dependent on the stress state and loading history (Zeng and Fang, 2025, 2023; Brünig et al., 2008; Shang et al., 2021; Wu et al., 2022; Tomstad et al., 2023), as it is mainly caused by the growth and coalescence of micro-voids under tension-dominated stress states. In contrast, under shear-dominated conditions, damage results from the growth and coalescence of micro-shear-cracks. It should be noted that micro-shear-cracks are also a form of micro-defect growth, but they occur mainly through isochoric deformation without significant volume changes. Thus, an anisotropic stress-state-dependent damage strain rate tensor was proposed by Brünig (2003) to characterize both volumetric and isochoric deformations of micro-defects, taking into account the loading history. In addition, using a tensor-based damage variable introduces anisotropy, allowing for the capture of different damage evolution behaviors under various loading directions. Most recently, Wei et al. (2023b) proposed a novel kinematic softening law by incorporating the tensor-based damage strain rate tensor (Brünig et al., 2008) into the kinematic hardening formulation developed by Frederick and Armstrong (2007), thereby enabling the characterization of the movement of the damage surface.

Non-proportional loading, induced by changes in loading directions, has been investigated using various testing specimens (Papasidero et al., 2015; Cortese et al., 2016; Gerke et al., 2019; Brünig et al., 2021; Iftikhar and Khan, 2021; Hou et al., 2022; Raj et al., 2022; Kong et al., 2023; Scales et al., 2019; Chen et al., 2019; Min et al., 2022; Hou et al., 2023). Papasidero et al. (2015) and Chen et al. (2019) experimentally and numerically analyzed the ductile damage and fracture behavior under non-proportional loading using a tension–torsion tubular specimen. Similarly, a tubular specimen was used by Cortese et al. (2016) to study the nonlinear accumulation of damage under non-proportional loading conditions. On the other hand, the cruciform biaxial specimen is another effective method to apply non-proportional loading by varying the loading ratio. Brünig et al. (2021) and Kong et al. (2023) studied how different preloads affect subsequent loading conditions using cruciform biaxially loaded specimens. Brünig et al. (2021) pointed out that pre-tensile loading followed by shear loading results in more brittle material behavior. Although the final loading stage is shear, the dominant damage mechanism remains void growth, in contrast to the micro-shear-crack mechanism typically observed in monotonic shear tests. A reduction in ductility under shear-to-tension loading patterns was also observed

by Kong et al. (2023). The aforementioned studies on non-proportional loading with different ductile metals and various testing specimens highlight that changes in the loading direction can significantly influence material behavior. However, it is worth noting that these studies primarily focus on a single change in loading direction and do not consider multiple changes in loading direction over time. On the other hand, most previous studies on ductile damage and fracture behavior under reverse loading are limited to conventional reversal cyclic loading patterns, where the loading direction switches from positive to negative (Kanvinde and Deierlein, 2007; Voyiadjis et al., 2013; Marcadet and Mohr, 2015; Daroju et al., 2022; Wu et al., 2024; Wei et al., 2025a; Yang et al., 2022; Frodal et al., 2019). They do not consider significant changes in loading modes, such as transitions from tension to shear or from shear to tension. Non-proportional cyclic loading with complex loading path changes under small plastic strains has been extensively studied in the field of fatigue damage, as reported in Song et al. (2017), Kang et al. (2005) and Wu (2018). However, in applications such as offshore wind structures or engineering structures subjected to earthquakes, materials are often subjected to large plastic deformations under non-proportional loading, which requires a different understanding of ductile damage behavior. This reveals a clear gap in the literature regarding the definition of new types of cyclic loading patterns, such as tension-to-shear cycles, with a focus on large plastic deformations to study ductile damage rather than fatigue damage, which is typically limited to small plastic strains.

In recent years, a series of uniaxial and biaxial reverse loading experiments have been conducted by Wei et al. (2022, 2023b,c, 2024a, 2025b) to investigate ductile damage and fracture behavior under various preload conditions, complex loading patterns, and different numbers of loading cycles. An example of experimental and numerical results for the previous biaxially loaded cyclic loading is briefly introduced in Appendix C. The main novelty of this paper lies in the introduction of a new type of cyclic loading without load reversal, achieved by multiple changes in loading direction. Both progressive and non-progressive cyclic loading patterns are investigated, including various tension-to-shear and shear-to-tension sequences. Since the experiments are still conducted within the framework of cyclic loading, the previously proposed cyclic plastic-damage continuum models remain applicable. However, some modifications are necessary, such as incorporating non-proportionality into the cyclic plasticity formulation to more accurately characterize plastic hardening. Moreover, since a large number of previous works (Brünig et al., 2021; Wei et al., 2022; Zistl et al., 2022; Wei et al., 2023b,c, 2024a, 2025b) have collected various SEM images taken from fracture surfaces under different loading conditions, it is now possible to establish a dataset. A machine learning tool is then used to identify and analyze the fracture surfaces quantitatively, in contrast to traditional visual assessment methods. In the present work, multi-layer convolutional neural networks (CNNs) are employed to characterize the fracture features. The convolutional operations in CNNs are effective at automatically extracting and selecting relevant features from input images, reducing the image size layer by layer. This makes CNNs particularly well suited to handling grid-like structured data, such as images, while using fewer neurons in the hidden layers compared to traditional fully connected artificial neural networks (ANNs) (Ansari, 2023). In addition, to observe the evolution of micro-defects inside the specimen in the fractured and unfractured regions, metallographic images are taken from different positions to compare potential differences in material behavior caused by ductile damage. These two analytical methods are newly introduced in the present work compared to previous studies, aiming to provide different perspectives for analyzing the newly designed and conducted non-proportional shear-tension cyclic experiments.

This paper is structured as follows: Section 2 describes the materials, newly designed experimental loading patterns, and the corresponding experimental setup. The previously proposed model and its modifications are discussed in Section 3. The numerical setup and the comparison between the original and the newly proposed models are presented in Section 4. In addition, the experimental and numerical results are discussed from different perspectives in Section 5. Finally, the conclusions are provided in Section 6.

2. Materials and experiments

The ductile aluminum alloy AW 6082-T6 provides high specific strength and good weldability and is widely used in structural and vehicle components. The details of the chemical composition are summarized in Table 1. Additionally, the microstructure of the investigated aluminum alloy AW 6082-T6 is statistically analyzed using Electron Backscatter Diffraction (EBSD). The EBSD analysis revealed no significant texture in the investigated material. A large number of experimental and numerical analyses of the investigated aluminum alloy have been performed under different proportional (Gerke et al., 2019) and non-proportional monotonic (Gerke et al., 2020; Brünig et al., 2021; Zistl et al., 2022) and cyclic loading conditions with large plastic strain amplitudes (Wei et al., 2022, 2023b, 2024a, 2025b). Previous cyclic experiments focused on applied symmetric cyclic loading with different cycle numbers, i.e., the magnitudes of the applied machine displacements in the tensile and compressive loading directions are approximately the same. The stress state is either maintained nearly constant due to different constant tensile or compressive preloads superimposed with shear cyclic loading using biaxially loaded specimens, as shown in the example load–displacement curves in Fig. C.21(d) and (f) and Fig. C.23 (Wei et al., 2023b, 2025b), or varies due to biaxial cyclic changes in loading direction along both axes simultaneously, resulting in stress states with approximately equal magnitudes in tension and compression (Wei et al., 2024a), as illustrated in Figs. C.21(e) and C.22 . A more detailed description of the previously designed experiments is briefly summarized in Appendix C. All experiments have in common that ductile fracture is triggered in fewer than 10 cycles. Inspired by progressive cyclic loading and non-proportional loading paths from tension-to-shear or shear-to-tension, which significantly change the loading direction during cyclic deformation, a new series of non-reverse progressive non-proportional experiments is proposed. The study focuses on analyzing the different effects of loading sequences and combinations of increasing displacement increments in tensile and shear loading patterns. In addition, several changes in loading between tension-dominated and shear-dominated

Table 1
Chemical composition of the aluminum alloy EN-AW 6082-T6 (AlSiMgMn) (Wei et al., 2022).

Al	Si	Mg	Mn	Fe	Cu	Zn	Ti	Others
to balance	0.90%	0.70%	0.47%	0.37%	0.09%	0.09%	0.03%	0.06%

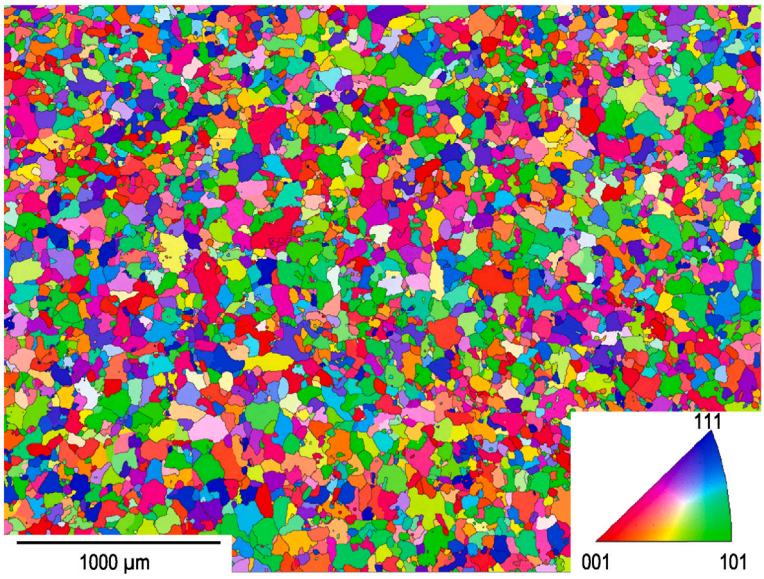

Fig. 1. Microstructure of the investigated aluminum alloy AW 6082-T6 analyzed using Electron Backscatter Diffraction (EBSD).

conditions result in multiple changes in damage mechanisms since tension and shear loading induce significantly different types of damage.

The H-specimen designed by Gerke et al. (2017) is used in this work. Its geometry is shown in Fig. 2(a), with symmetric notches and a specimen thickness of 4 mm. The notch details are shown in Fig. 2(c). In addition, the cross-section A-A of the notch is shown in Fig. 2(d), with a notch radius of 2 mm and a resulting notch depth of 2 mm. As illustrated in Fig. 2(e), different stress states are induced along different axes: applying machine displacement u_1^M along axis 1 results in shear loading, whereas applying machine displacement u_2^M along axis 2 induces tension loading. Thus, different combinations of machine displacement u_1^M and machine displacement u_2^M lead to a wide range of stress states. In this work, the experiments are divided into two groups: cyclic loading following a tension-to-shear progressive pattern and a shear-to-tension pattern, namely cyc-TS and cyc-ST. Note that the progressive loading patterns refer to increasing relative machine displacement increments, i.e., Δu^M increases compared to the previous loading cycles. For both experimental and numerical analysis, the relative displacement $\Delta u_{\mathrm{ref,i}}$ and the mean force F_i are defined based on the gauge points indicated by the red circles in Fig. 2(e). They are given by

$$\Delta u_{\mathrm{ref,i}} = u_{i,1} + u_{i,2} \quad \text{and} \quad F_i = \frac{F_{i,1} + F_{i,2}}{2}, \tag{1}$$

respectively. It should be mentioned that the gauge points along axis 1 are defined by the intersections of the bottom line and the upper line of the specimen in axis 2 with the symmetric line of the specimen in the vertical direction, respectively. In contrast, the gauge points along axis 2 are defined along the symmetric horizontal axis at a location 2 mm from the edge of the central opening, as indicated by the dashed line in Fig. 2(e).

Since the fracture machine displacement Δu^M in the tensile direction is significantly smaller than in the shear direction, machine displacement increments of $\Delta u_2^M = 0.05$ mm and 0.1 mm are used in the tensile direction, whereas $\Delta u_1^M = 0$ mm, 0.1 mm, 0.15 mm, and 0.25 mm are used in the shear loading direction. For each different cyclic loading pattern, the first loading increment in the tensile direction is $\Delta u_2^M = 0.65$ mm, and $\Delta u_1^M = 0.6$ mm in the shear direction, followed by a third loading pattern with respective loading increments depending on the loading case. For the naming conventions, each test label consists of three parts: cyc/mon-TS/ST-Δu_2^M Δu_1^M / Δu_1^M Δu_2^M. The first part indicates the loading type, either monotonic (mon) or cyclic (cyc). The second part denotes the loading sequence, where S indicates shear and T indicates tension. The third numeric part represents the relative increase in machine displacement Δu^M corresponding to the specified loading sequence. The classification of the newly proposed experiments is listed in Table 2. The relative displacement–time under cyclic loading conditions are shown in Fig. D.25. All experiments are conducted under displacement-controlled conditions. However, for the unloading path, a stopping criterion must be defined to ensure that the resulting end force is close to zero. Consequently, the required unloading displacement becomes an unknown variable. Based on experimental observations, this required machine displacement is generally smaller than the designed displacement used during

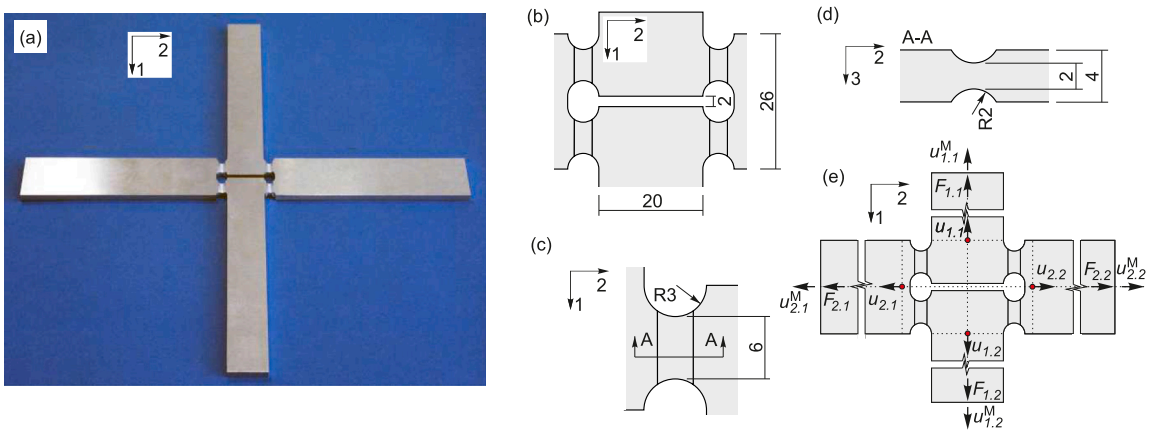

Fig. 2. Cruciform biaxially loaded H-specimen made from a 4 mm thick metal sheet: (a) isometric photo of the H-specimen, (b)–(c) details of the central opening and the corresponding notch regions, (e) loading and measurement points; all units in mm.

Table 2
The classification for the non-proportional progressive shear-tension cyclic loading experiments.

Machine displacements for the monotonic loading or the first cyclic loading pattern								
Tests	u_1^M [mm]	u_2^M [mm]	Tests	u_2^M [mm]	u_1^M [mm]	Tests	u_1^M [mm]	u_2^M [mm]
mon-T	n.a.	until fracture	cyc-TS	0.65	0.6	cyc-ST	0.6	0.65
mon-S	until fracture	n.a.						
Increments of machine displacement for subsequent cyclic loading patterns follow the naming convention: cyc-TS/ST-Δu_2^M $\Delta u_1^M/\Delta u_1^M$ Δu_2^M								
Tests	Δu_2^M [mm]	Δu_1^M [mm]	Tests	Δu_2^M [mm]	Δu_1^M [mm]	Tests	Δu_1^M [mm]	Δu_2^M [mm]
cyc-TS-T0.05S0	0.05	0	cyc-TS-T0.1S0	0.1	0	cyc-ST-S0.15T0.05	0.15	0.05
cyc-TS-T0.05S0.1	0.05	0.1	cyc-TS-T0.1S0.1	0.1	0.1	cyc-ST-S0.15T0.1	0.15	0.1
cyc-TS-T0.05S0.15	0.05	0.15	cyc-TS-T0.1S0.15	0.1	0.15	cyc-ST-S0.25T0.1	0.25	0.1

the loading stage. Furthermore, during machine displacement applied along one loading axis, a slight movement may also be induced in the other axis. For example, when loading is applied along axis 2, the relative displacement along axis 1 also exhibits a nonlinear increase, as observed in Fig. D.25.

The newly designed biaxial non-proportional progressive shear-tension cyclic loading experiments were performed using a horizontally arranged electro-mechanical testing machine, LFM-BIAX 20 kN, manufactured by Walter + Bai AG, Switzerland. The tests were conducted under static loading conditions with a loading speed of 0.004 mm/s, and all experiments were repeated three times to obtain consistent results. Based on the experimental measurements, the corresponding strain rate is approximately $0.0004\,s^{-1}$. The samples are manufactured from a 4 mm thick metal sheet without surface polishing. Each specimen is milled from the sheet metal with a design tolerance of ±0.02 mm. Due to the use of the DIC technique, all specimens are first sprayed with white acrylic paint and subsequently coated with graphite to produce a black speckle pattern. According to the DIC system manufacturer's guidelines and the recommendations in the *A Good Practices Guide for Digital Image Correlation* (Jones and Iadicola, 2018), the required speckle size should range between 3 and 5 pixels. Four 6 MPx cameras equipped with 75 mm lenses are positioned above and below the specimen, with sufficient LED lighting, as shown in Fig. 3(a). It should be noted that the camera objectives above and below the H-specimen are symmetrically aligned and positioned along the same vertical axis. A detailed view of the biaxial testing device with the testing specimen and respective axial positions is shown in Fig. 3(b), and the axial positions correspond to the loading and measurement point coordinates illustrated in Fig. 2(e). For the DIC setup, the image acquisition frequency is set to 1 Hz, and the subset size and grid spacing are chosen as 33×33 pixels and 11 pixel, respectively, for data evaluation. In addition, the region of interest is defined as 2752×2206 pixels, and the average resolution at the center of the H-specimen is approximately 60 pixel/mm.

After the experiments, as depicted in Fig. 4, the selected fracture surface (N2) will be used to analyze the respective damage mechanisms using a scanning electron microscope (SEM). The size and number of micro-defects in the fractured (N1) and unfractured notches (N3) will be quantitatively analyzed using a light optical microscope (LOM). For SEM analysis, representative images of the notched cross-section will be taken at three positions, the left, right, and middle parts of the fracture surface, to analyze the corresponding damage mechanisms. On the other hand, the middle layer of the notch surface is prepared for imaging using an optical microscope. The goal of the optical analysis of the specimen after failure, at both the fractured and unfractured notches, is to determine whether micro-defects have developed or deformed and to compensate for the limitations of SEM in observing damage behavior.

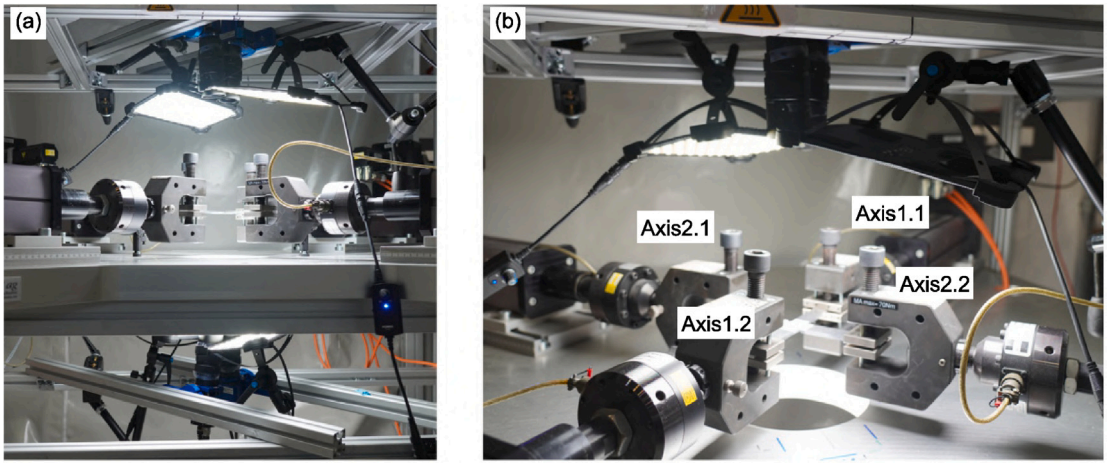

Fig. 3. Biaxial testing device and digital image correlation (DIC) setup, including cameras and lighting systems.

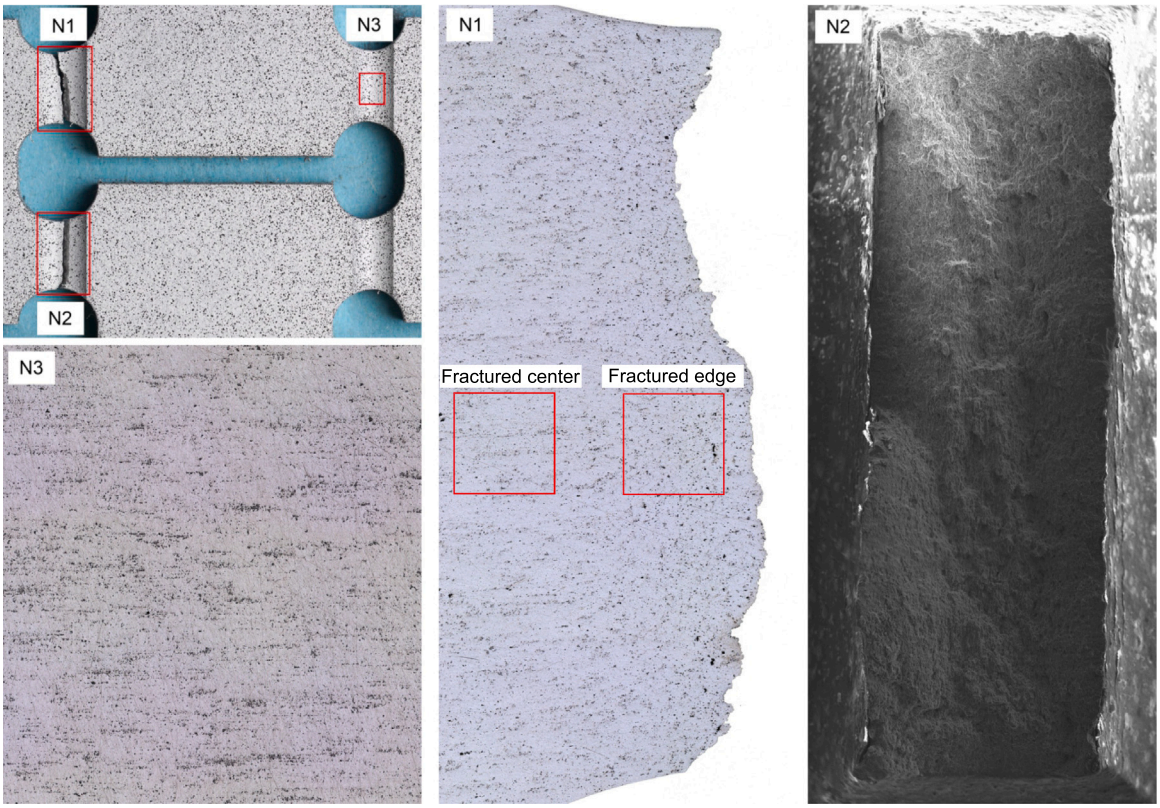

Fig. 4. Schematic illustration of the selected notched region for SEM and LOM analysis. N1 refers to the fractured notch edge, N2 indicates the fracture surface, and N3 represents the unfractured region.

3. Constitutive model

The two-surface cyclic plastic-damage constitutive model, incorporating the stress differential (SD) effect, the non-hardening effect, and the Bauschinger effect, was introduced by Wei et al. (2023b). This model has been applied to various complex cyclic loading conditions (Wei et al., 2024a, 2025a,b), providing accurate predictions of local strains and damage evolution when compared with experimental results. Since strain-hardening behavior changes significantly with repeated changes in loading direction, such as from tension-to-shear or shear-to-tension, and considering the ratcheting effect, strain hardening under non-proportional loading

must be incorporated into the constitutive model to more accurately reflect material behavior. In this section, the model is briefly summarized, and the new modifications to the isotropic and kinematic hardening laws, which capture the strain hardening under non-proportional loading, are presented in detail.

3.1. Cyclic plasticity and damage model

The framework follows the kinematics introduced by Brünig (2003). The effective fictitious undamaged configuration captures only the elastic–plastic behavior, while the elastic–plastic-damage behavior is characterized in the damage configuration. A brief summary of the kinematic framework is provided in the Appendix A. Accordingly, in this paper, all tensors with a superscript bar symbol refer to quantities in the effective fictitious undamaged configuration, whereas standard (unbarred) tensors refer to quantities in the damage configuration.

In the effective undamaged configuration, the effective strain rate tensor $\dot{\bar{\mathbf{H}}}$ is additively decomposed into an elastic $\dot{\bar{\mathbf{H}}}^{\mathrm{pl}}$ and plastic part $\dot{\bar{\mathbf{H}}}^{\mathrm{el}}$

$$\dot{\bar{\mathbf{H}}} = \dot{\bar{\mathbf{H}}}^{\mathrm{el}} + \dot{\bar{\mathbf{H}}}^{\mathrm{pl}}\,. \tag{2}$$

Similarly, the total strain rate tensor is expressed as

$$\dot{\mathbf{H}} = \dot{\mathbf{H}}^{\mathrm{el}} + \mathbf{R}^{-1}\dot{\bar{\mathbf{H}}}^{\mathrm{pl}}\mathbf{R} + \mathbf{Q}^{\mathrm{el}-1}\dot{\mathbf{H}}^{\mathrm{da}}\mathbf{Q}^{\mathrm{el}}\,, \tag{3}$$

where $\dot{\mathbf{H}}^{\mathrm{da}}$ is the damage strain rate tensor, $\mathbf{R}$ denotes the damage tensor, and $\mathbf{Q}^{\mathrm{el}}$ represents the elastic part of the metric transformation tensor. Details of the derivation can be found in Appendix A.

Within the framework of the effective fictitious undamaged configuration, constitutive equations are developed to represent the elastic–plastic response of the undamaged matrix material accurately. Considering the asymmetric yield surface and the Bauschinger effect, the Drucker–Prager-type yield condition is used to characterize the onset of yielding (Wei et al., 2023b)

$$f^{\mathrm{pl}} = \sqrt{\frac{1}{2}\mathrm{dev}(\bar{\mathbf{T}}-\bar{\boldsymbol{\alpha}})\cdot\mathrm{dev}(\bar{\mathbf{T}}-\bar{\boldsymbol{\alpha}})} - \bar{c}\left(1-\frac{a}{\bar{c}}\,\mathrm{tr}(\bar{\mathbf{T}}-\bar{\boldsymbol{\alpha}})\right) \quad = \sqrt{\bar{J}_2} - \bar{c}(1-\frac{a}{\bar{c}}\,\bar{I}_1) = 0\,, \tag{4}$$

where $\bar{\mathbf{T}}$ and $\bar{\boldsymbol{\alpha}}$ are the effective Kirchhoff stress tensor and the effective back stress tensor in the effective fictitious undamaged configurations, respectively, $\bar{c}$ describes the effective equivalent stress, and $a/\bar{c}$ represents the constant hydrostatic stress coefficient. The effective reduced stress invariants $\bar{I}_1$ and $\bar{J}_2$ are calculated based on the effective reduced stress tensor $\bar{\mathbf{T}}-\bar{\boldsymbol{\alpha}}$. In addition, the effective Kirchhoff stress, describing the undamaged material state, is defined as

$$\bar{\mathbf{T}} = (\bar{T})^{i}_{\ j}\mathbf{g}_i\otimes\mathbf{g}^j = 2G\mathbf{A}^{\mathrm{el}} + \left(K-\frac{2}{3}G\right)\mathrm{tr}\,\mathbf{A}^{\mathrm{el}}\mathbf{1}\,, \tag{5}$$

where G and K are the shear and bulk modulus, $\mathbf{A}^{\mathrm{el}}$ denotes the logarithmic elastic strain tensor, and $\mathbf{1}$ represents the second-order identity tensor.

Although the hydrostatic stress evidently influences the onset of plastic yielding, it has a negligible effect on plastic strains, since there is no volume change due to plastic deformation (Spitzig and Richmond, 1984; Brünig, 2003). Thus, it leads to the non-associated plastic flow rule

$$\dot{\bar{\mathbf{H}}}^{\mathrm{pl}} = \dot{\lambda}\frac{1}{2\sqrt{\bar{J}_2}}\,\mathrm{dev}(\bar{\mathbf{T}}-\bar{\boldsymbol{\alpha}}) = \dot{\gamma}\bar{\mathbf{N}} \tag{6}$$

with a non-negative factor $\dot{\lambda}$, the rate of the equivalent plastic strain $\dot{\gamma} = \dot{\lambda}/\sqrt{2}$, and the effective deviatoric normalized reduced stress direction $\bar{\mathbf{N}}$. It should be noted that, in the proposed theoretical framework, micro-void growth is governed by the damage strain rate tensor $\dot{\mathbf{H}}^{\mathrm{da}}$, rather than by the plastic strain rate tensor $\dot{\bar{\mathbf{H}}}^{\mathrm{pl}}$.

In the damaged configuration, the framework characterizes the kinematics of anisotropic damage. To characterize the stress-state-dependent onset of damage behavior, the damage condition is given by

$$f^{\mathrm{da}} = \hat{\alpha}^{\mathrm{da}}\,\mathrm{tr}(\mathbf{T}-\boldsymbol{\alpha}) + \hat{\beta}^{\mathrm{da}}\sqrt{\frac{1}{2}\mathrm{dev}(\mathbf{T}-\boldsymbol{\alpha})\cdot\mathrm{dev}(\mathbf{T}-\boldsymbol{\alpha})} - \tilde{\sigma} \quad = \hat{\alpha}^{\mathrm{da}}\tilde{I}_1 + \hat{\beta}^{\mathrm{da}}\sqrt{\tilde{J}_2} - \tilde{\sigma} = 0\,, \tag{7}$$

where $\mathbf{T}$ and $\boldsymbol{\alpha}$ are the Kirchhoff stress tensor and the damage back stress tensor, respectively, and $\tilde{I}_1$ and $\tilde{J}_2$ represent the first and second deviatoric reduced stress invariants, respectively. In addition, $\hat{\alpha}^{\mathrm{da}}$ and $\hat{\beta}^{\mathrm{da}}$ denote the stress-state-dependent coefficients (Brünig et al., 2013, 2016)

$$\hat{\alpha}^{\mathrm{da}} = \begin{cases} 0 & \text{for} \quad \eta \le 0 \\ \frac{1}{3} & \text{for} \quad \eta > 0 \end{cases}$$
$$\hat{\beta}^{\mathrm{da}}(\eta,\omega) = -0.017\omega^3 - 0.065\omega^2 - 0.078\omega - 1.28\eta + 0.85 \ge 0\,, \tag{8}$$

respectively, with the stress triaxiality

$$\eta = \frac{\sigma_{\mathrm{m}}}{\sigma_{\mathrm{eq}}} = \frac{I_1}{3\sqrt{3J_2}}\,, \tag{9}$$

and the stress Lode parameter

$$\omega = \frac{2T_2 - T_1 - T_3}{T_1 - T_3} \quad \text{with the principal stresses} \quad T_1 \geq T_2 \geq T_3\,, \tag{10}$$

where σ_{m} and σ_{eq} denote the mean stress and the von Mises equivalent stress, respectively, both calculated from the Kirchhoff stress tensor $\mathbf{T}$. Compared to the effective Kirchhoff stress tensor $\bar{\mathbf{T}}$ (5), the Kirchhoff stress tensor $\mathbf{T}$ considering elastic degradation parameters $\eta_1 ... \eta_4$ and the damage strain tensor $\mathbf{A}^{\mathrm{da}}$ is defined as

$$\mathbf{T} = (T)^i_{\ j}\mathbf{g}_i \otimes \mathbf{g}^j = 2(G + \eta_2 \mathrm{tr}\mathbf{A}^{\mathrm{da}})\mathbf{A}^{\mathrm{el}} + \left[(K - \frac{2}{3}G + 2\eta_1 \mathrm{tr}\mathbf{A}^{\mathrm{da}})\mathrm{tr}\mathbf{A}^{\mathrm{el}} + \eta_3(\mathbf{A}^{\mathrm{da}} \cdot \mathbf{A}^{\mathrm{el}})\right]\mathbf{1} + \eta_3 \mathrm{tr}\mathbf{A}^{\mathrm{el}}\mathbf{A}^{\mathrm{da}} + \eta_4(\mathbf{A}^{\mathrm{el}}\mathbf{A}^{\mathrm{da}} + \mathbf{A}^{\mathrm{da}}\mathbf{A}^{\mathrm{el}})\,. \tag{11}$$

The incorporation of the damage tensor into the effective Kirchhoff stress (5) enables the characterization of elastic degradation induced by micro-defects. In addition, the damage strain tensor is defined as the logarithm of the damage tensor

$$\mathbf{A}^{\mathrm{da}} = (A^{\mathrm{da}})^i_{\ j}\mathbf{g}_i \otimes \mathbf{g}^j = \frac{1}{2}\ln \overset{*}{\mathbf{R}}\,, \tag{12}$$

where $\overset{*}{\mathbf{R}}$ is the current damage metric deformation tensor, describing the kinematic relation between the effective undamaged configuration and the damaged configuration. The details of the proposed kinematics are described in Appendix A. It should be mentioned that, for the numerical implementation, the damage strain rate tensor is first calculated. Based on the previously computed damage strain tensor, the current damage strain tensor is then updated. For more details on the implementation, see Wei et al. (2024b).

Furthermore, the damage strain rate tensor is expressed in the form of

$$\dot{\mathbf{H}}^{\mathrm{da}} = \dot{\mu}(\tilde{\alpha}^{\mathrm{da}}\frac{1}{\sqrt{3}}\mathbf{1} + \tilde{\beta}^{\mathrm{da}}\tilde{\mathbf{N}})\,, \tag{13}$$

where $\dot{\mu}$ describes the rate of the equivalent damage strain, $\tilde{\mathbf{N}}$ represents the normalized transformed reduced stress tensor. The above mathematical formulation of the damage strain rate tensor incorporates directional anisotropy, as it describes both the volumetric and isochoric deformation of micro-defects while accounting for stress-state dependence. In addition, $\tilde{\alpha}^{\mathrm{da}}$ and $\tilde{\beta}^{\mathrm{da}}$ are stress-state-dependent coefficients (Brünig et al., 2013, 2016)

$$\tilde{\alpha}^{\mathrm{da}}(\eta) = \begin{cases} 0 & \text{for} \quad \eta \leq 0 \\ 0.5714\eta \leq 1 & \text{for} \quad \eta > 0 \end{cases}, \tag{14}$$

and

$$\tilde{\beta}^{\mathrm{da}}(\eta, \omega) = \tilde{\beta}_0(\eta) + \begin{cases} (1 - \omega^2)(0.0378\eta - 0.0252) & \text{for} \quad \eta \leq 2/3 \\ 0 & \text{for} \quad \eta > 2/3 \end{cases} \tag{15}$$

with

$$\tilde{\beta}_0(\eta) = \begin{cases} 0.87 & \text{for} \quad \eta \leq 1/3 \\ 0.97875 - 0.32625\eta \geq 0 & \text{for} \quad \eta > 1/3 \end{cases}, \tag{16}$$

respectively. The stress-state-dependent damage parameters are identified by analyzing a unit cell containing a centrally located micro-void. Various loading conditions are applied to the unit cell to generate different stress states. Based on the kinematic relations within the unit cell, the corresponding damage strain tensor can be calculated. This enables the calibration of a mathematical formulation that captures the dependence of damage evolution on the stress state (Brünig et al., 2013). The obtained material parameters have been applied to both steel and the investigated aluminum alloy, providing accurate predictions of the material's damage behavior.

3.2. Hardening laws

In the present work, the combined hardening law is used to capture the strain hardening under reverse loading conditions, formulated as a linear combination of the respective isotropic and kinematic laws with a scalar hardening ratio ρ_h. The Voce-type isotropic hardening law is introduced to characterize the change in the size of the yield surface. In addition, Wei et al. (2022) proposed a double-term, strain-state-dependent (η_{A}) Voce hardening model to describe the elastic–plastic transition under various loading conditions more accurately. On the other hand, the modified Chaboche kinematic hardening model is introduced to predict the movement of the yield surface under large plastic strain deformations, incorporating an angle parameter to control the nonlinear behavior of kinematic hardening. In further research, Wei et al. (2023b) indicated that isotropic and kinematic hardening change after shear reverse loading. This so-called non-hardening effect refers to a condition where, after shear reversal within a certain plastic region, only kinematic hardening remains. Compared to the previous hardening model, a nonlinearity parameter related to characterizing the change in loading direction under progressive cyclic loading conditions is newly introduced into the isotropic and kinematic hardening laws.

To characterize proportional and non-proportional loading, two angle-based parameters are commonly used in the literature (Benallal and Marquis, 1987; Tanaka, 1994). The approach proposed by Benallal and Marquis (1987) defines the parameter based on the plastic strain increment $\mathrm{d}\boldsymbol{\varepsilon}^p$ and the angle between the directions of the deviatoric stress increments $\mathrm{d}\mathbf{S}$, and it is given by

$$A = \sqrt{1 - \cos^2\theta} = \sqrt{1 - \frac{\mathrm{d}\mathbf{S} \cdot \mathrm{d}\boldsymbol{\varepsilon}^p}{\|\mathrm{d}\mathbf{S}\|\ \|\mathrm{d}\boldsymbol{\varepsilon}^p\|}} \tag{17}$$

However, as noted by Jiang and Kurath (1997) and Kang et al. (2005), the Benallal approach to quantifying non-proportionality is inadequate for certain strain paths, such as the butterfly path. Compared to the Benallal and Marquis approach, Tanaka (1994) introduced a more complex fourth-order tensor dependent on a memory quantity to track non-proportionality. Calloch and Marquis (1999) indicated that both methods provided good results, but the Tanaka approach yielded more robust outcomes compared to the angle parameter proposed by Benallal and Marquis (1987). Skibicki et al. (2022) numerically analyzed experiments under a wide range of multiaxial asynchronous loading conditions using Tanaka's non-proportionality parameter within a cyclic plasticity model, and confirmed its accuracy. Moreover, Wu (2018) indicated that the Benallal and Marquis approach can accurately predict cross hardening conditions involving sudden changes in the principal directions. Due to the simplicity of the mathematical formulation of the Benallal and Marquis model, as also mentioned by Kang et al. (2005), and its suitability for tension-to-shear and tension-to-shear loading path changes, the Benallal-type formulation is adopted in the present work.

Furthermore, inspired by Benallal and Marquis (1987), Wei et al. (2022) modified the formulation of the angle parameter by using the deviatoric effective reduced stress tensor $\bar{\mathbf{T}} - \bar{\boldsymbol{\alpha}}$ in Eq. (4) and the third component of the effective back stress tensor $\bar{\boldsymbol{\alpha}}_3$ to characterize non-proportionality caused by large deformations. This modification incorporates the effective back stress tensor through a combined hardening model under both monotonic and cyclic loading conditions, enabling a more accurate representation of non-proportionality effects. The modified angle parameter is defined as

$$\theta_a = 1 - \cos^2\theta = 1 - \frac{((\bar{\mathbf{T}} - \bar{\boldsymbol{\alpha}}) \cdot \bar{\boldsymbol{\alpha}}_3)^2}{\|\bar{\mathbf{T}} - \bar{\boldsymbol{\alpha}}\| \, \|\bar{\boldsymbol{\alpha}}_3\|} \tag{18}$$

It has been shown that the modified angle parameter remains nearly constant at a value close to zero during monotonic and cyclic uniaxial tension tests, with only slight variation shortly before fracture. In contrast, the non-proportionality under monotonic shear loading with large plastic deformation is significantly greater than in uniaxial tension tests. By introducing the angle parameter only in the third term of the Chaboche kinematic hardening model, the performance of the modified model under large plastic deformations is significantly improved, see Wei et al. (2022). Building on this success in modeling non-proportionality due to large plastic deformation, the approach has also been shown to effectively capture the material response under non-proportional loading, as investigated in the present work, by varying the loading direction between tension and shear. Thus, the modified angle parameter is newly incorporated into the isotropic and kinematic hardening laws to model the change in hardening behavior under non-proportional loading conditions.

Considering the non-proportionality effect, the modified triple-term Voce strain hardening law

$$\bar{c} = c_0 + Q_1(1 - e^{-p_1\gamma}) + Q_2(1 - \theta_b)\xi(1 - e^{-p_2\gamma}) + Q_3\theta_b(1 - e^{-p_3\gamma}) \tag{19}$$

is employed to more accurately capture the evolution of isotropic hardening, where c_0 describes the initial yield stress, and $Q_1..Q_3$, ξ, and $p_1...p_3$ are material constants. It is assumed that the angle parameter only affects the second term of the Voce hardening law, since the material response is significantly influenced by non-proportionality during the elastic–plastic transition stage. For proportional loading, $\theta_a = 0$, whereas for non-proportional loading, θ_a lies between 0 and 1. A value close to 1 indicates a high degree of non-proportionality. To better characterize non-proportional loading and emphasize its influence on the material response, the coefficient θ_b is formulated in the form of

$$\theta_b = \begin{cases} (\theta_a)^2 & \text{for} \quad \theta_a \leq \frac{1}{2} \\ \theta_a & \text{for} \quad \theta_a > \frac{1}{2} \end{cases}, \tag{20}$$

A threshold value of 1/2 is introduced based on numerical observations, which more accurately capture the strain hardening behavior in the non-proportional loading regime. This strain hardening effect is expected to vanish after a certain range following a change in the loading direction. Therefore, a relation of $\theta_b = (\theta_a)^2$ is suggested. It is evident that the third term of the Voce hardening is omitted under proportional loading with the angle parameter $\theta_b = 0$. Moreover, although θ_b can be slightly greater than zero under monotonic large plastic deformations, the influence of the third term ($Q_3\theta_b(1 - e^{-p_3\gamma})$) on the hardening behavior is negligible.

Similarly, by introducing an evolution rule of kinematic hardening based on the angle parameter θ_b, the modified Chaboche kinematic hardening law can be defined as

$$\dot{\bar{\boldsymbol{\alpha}}}_1 = b_1^m \dot{\bar{\mathbf{H}}}^{\mathrm{pl}} - b_2\chi\dot{\gamma}\bar{\boldsymbol{\alpha}}_1\,, \quad \dot{\bar{\boldsymbol{\alpha}}}_2 = b_3 \dot{\bar{\mathbf{H}}}^{\mathrm{pl}} - b_4\dot{\gamma}\bar{\boldsymbol{\alpha}}_2\,, \quad \text{and} \quad \dot{\bar{\boldsymbol{\alpha}}}_3 = b_5 \dot{\bar{\mathbf{H}}}^{\mathrm{pl}} - b_6\dot{\gamma}\theta_a\bar{\boldsymbol{\alpha}}_3 \tag{21}$$

with

$$b_1^m = b_1\chi(1 - \theta_b) + b_1^{inf}\theta_b \qquad \text{and} \qquad b_1^{inf} = \frac{b_7}{\kappa(\gamma)}\,, \tag{22}$$

where $b_1...b_7$ are material constants, and $\chi = 0.8e^{-300\gamma} + 0.2$ represents the exponential decay function. Again, the non-proportionality due to the change in loading direction significantly influences the elastic–plastic transition; thus, the kinematic hardening evolution law is applied only to the first term of the kinematic hardening law $\dot{\bar{\boldsymbol{\alpha}}}_1$. The definition of b_1^m follows the work of Jiang and Kurath (1997) and Kang et al. (2005), where the hardening term b_1^{inf} is activated by strain hardening under non-proportional loading conditions. The evolution of this hardening effect is designed to exhibit a decaying trend until it vanishes, governed by the angle θ_b and a decay function $1/\kappa(\gamma)$ based on the equivalent plastic strain γ. The corresponding formulation should be inversely fitted using experimental data. It is worth mentioning that the angle parameter θ_a (Eq. (18)) remains unchanged from previous work (Wei et al., 2022, 2023b), as the third term of the effective back stress contributes less to the evolution of the total effective back stress

in the elastic–plastic transition region compared to the first and second terms. Therefore, the functional form in Eq. (20) is not reconsidered. Additionally, the non-proportionality induced by large deformation is considerably smaller than that caused by a sudden changes in loading direction.

The combined hardening law is based on a linear combination of the rate of the equivalent effective stress $\dot{\bar{c}}$ and the rate of the effective back stress tensor $\dot{\bar{\alpha}}$ in terms of the isotropic hardening ratio ρ_h

$$\dot{\bar{\sigma}} = k_h \rho_h \dot{\bar{c}} + (1 - k_h \rho_h) \dot{\bar{\alpha}} \,, \tag{23}$$

where $\dot{\bar{\sigma}}$ is the equivalent total hardening rate, and k_h is a function-based non-hardening effect parameter. The details and formulation are discussed in Wei et al. (2023b).

3.3. Laws of damage-induced softening in damage configurations

The laws damage-induced softening used in the damage configurations are the same as those presented in Wei et al. (2023b). A summary is provided here. Similar to the combined hardening concept, the combined softening also uses a damage softening parameter ρ_s, assumed to be the same as the isotropic hardening ratio ρ_h, and is given by

$$\dot{\sigma} = \rho_s \dot{\bar{\sigma}} + (1 - \rho_s) \dot{\alpha}_{\mathrm{eq}} \,, \tag{24}$$

where $\dot{\sigma}$ is the equivalent total softening rate, and $\dot{\bar{\sigma}}$ and $\dot{\alpha}_{\mathrm{eq}}$ denote the rates of the equivalent damage stress and damage back stress, respectively.

Moreover, the isotropic softening is computed in the form of an exponential function

$$\tilde{\sigma} = \tilde{\sigma}_0 - C_1 e^{-C_2 \mu} \tag{25}$$

with the initial damage stress $\tilde{\sigma}_0$, constant parameters C_1 and C_2, and the equivalent damage strain μ.

The kinematic softening law based on the damage strain rate tensor $\dot{\mathbf{H}}^{\mathrm{da}}$ in Eq. (13) was first proposed by Wei et al. (2023b), and follows the structure of Frederick–Armstrong's kinematic hardening law (Frederick and Armstrong, 2007). Thus, the rate of damage back stress tensor in the damage configurations is expressed as

$$\dot{\boldsymbol{\alpha}} = d_1 \dot{\mathbf{H}}^{\mathrm{da}} - d_2 \dot{\mu} \boldsymbol{\alpha} \,, \tag{26}$$

where d_1 and d_2 are softening material constants.

4. Numerical study of the non-proportionality parameters and strain hardening under non-proportional loading

4.1. Numerical setups

The proposed constitutive model has been implemented as a user-defined subroutine in Ansys, and the numerical integration has been discussed in detail in Wei et al. (2024b). The used material parameters are summarized in Table 3, and the details of the material identification are discussed in Wei et al. (2025a). A brief summary of the identification procedure for the basic elastic and plastic hardening parameters, determined using uniaxial tension and shear tests, is given in Appendix B. The validation of the identified parameters is presented in Figs. C.21, C.22, and C.23 for different complex biaxial loading paths. For the numerical calculations, one-quarter of the H-specimen is used due to its symmetry, as shown in Fig. 5(a). Solid185 elements with default settings are used, counting 22 061 elements. A refined mesh is applied in the notch region with a mesh size of $0.25\,\mathrm{mm} \times 0.125\,\mathrm{mm} \times 0.1\,\mathrm{mm}$ along axes 1, 2, and 3, as shown in Fig. 5(b). The mesh size used here has also been employed in previous work (Wei et al., 2023b, 2024b), and was determined through a mesh sensitivity study by comparing force–displacement curves and local strain fields with experimental results obtained under the same DIC settings, as described in Section 2. It provides stable and highly accurate results compared to the experimental data, especially in capturing the width of the shear band (Wei et al., 2025a). It is worth mentioning that the proposed local continuum damage model exhibits mesh dependence in the numerical results. However, this issue can be minimized by using a specific specimen mesh size along with an appropriate DIC setup. In addition, Fig. 5(c) shows the notch area, which is used to characterize the mean stress state, i.e., $\bar{\eta}$ and $\bar{\omega}$, which are defined as

$$\bar{\eta} = \frac{1}{S} \iint_S \eta \, ds \quad \text{and} \quad \bar{\omega} = \frac{1}{S} \iint_S \omega \, ds \,, \tag{27}$$

where S denotes the total area of the notched cross-section, marked by the red rectangle in Fig. 5(c).

4.2. Non-proportionality parameters

To numerically capture the change in loading direction using the proposed angle parameter, the angle parameters θ_a and θ_b are analyzed in detail based on their mean values $\bar{\theta}_a$ and $\bar{\theta}_b$ at the notched cross-section surface, as defined by the stress state. The respective mean angles $\bar{\theta}_a$ and $\bar{\theta}_b$ are computed as

$$\bar{\theta}_a = \frac{1}{S} \iint_S \theta_a \, ds \quad \text{and} \quad \bar{\theta}_b = \frac{1}{S} \iint_S \theta_b \, ds \,. \tag{28}$$

Table 3
Elastic, plastic and damage material parameters.

Symbol	Description	Value and unit	Symbol	Description	Value and unit
E	Young's modulus	67 500 MPa	b_2	Kinematic hardening constant	1750
ν	Poisson ratio	0.3	b_3	Kinematic hardening modulus	895 MPa
$\eta_1 \ldots \eta_4$	Elastic damage moduli	−10 000 MPa	b_4	Kinematic hardening constant	15
a/c	Hydrostatic stress coefficient	32 $^1/_{\text{TPa}}$	b_5	Kinematic hardening modulus	115 MPa
c_0	Initial yield stress	139 MPa	b_6	Kinematic hardening constant	7.5
Q_1	Isotropic hardening modulus	74.93 MPa	b_7	Kinematic hardening modulus	40 000 MPa
Q_2	Isotropic hardening modulus	21.31 MPa	$^1/_{\kappa(\gamma)}$	Decay function	$1/(1+1.67e^{-6.63\gamma})$
Q_3	Isotropic hardening modulus	190.58 MPa	$\tilde{\sigma}_0$	Initial equivalent damage stress	270 MPa
p_1	Isotropic hardening exponent	8.96	C_1	Isotropic softening modulus	0.004207 MPa
p_2	Isotropic hardening exponent	676.01	C_2	Isotropic softening exponent	92.97
p_3	Isotropic hardening exponent	39.6	d_1	Kinematic softening modulus	−0.51 MPa
b_1	Kinematic hardening modulus	61 250 MPa	d_2	Kinematic softening constant	−84

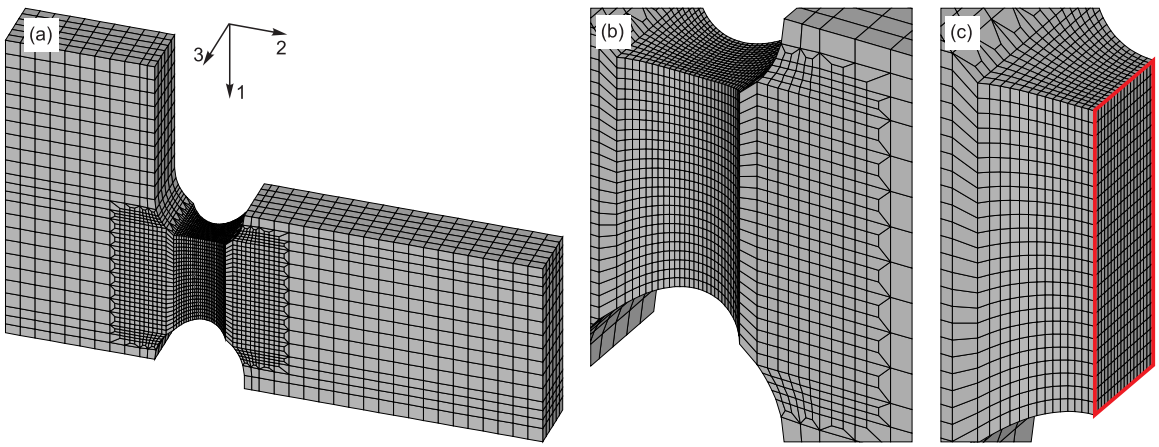

Fig. 5. (a) Overview of the H-specimen, (b) details of the refined mesh in the notch regions, and (c) notched cross-section.

It can be observed that $\bar{\theta}_a$ and $\bar{\theta}_b$ remain nearly zero during the monotonic tension tests (mon-T), whereas the value of $\bar{\theta}_a$ under monotonic shear loading (mon-S) slightly increases from 0 to 0.1 after the relative displacement $\Delta u_{1,\text{ref}}$ reaches 1 mm. As discussed in Wei et al. (2022), this slight increase activates the nonlinear term in the third effective back stress component in Eq. (21) under large deformation, resulting in a more accurate prediction of the kinematic hardening behavior. However, strain hardening under non-proportional loading is not intended to be introduced under monotonic proportional loading conditions. Therefore, a physical function for θ_b is proposed in Eq. (20) to minimize this value. As shown, the resulting value becomes relatively small, approximately 0.01. In the non-proportional loading case, the angle parameter $\bar{\theta}_a$ is evaluated before the change in loading direction from tension-to-shear (TS), as shown in Fig. 6(c), or from shear-to-tension (ST), as shown in Fig. 6(d), as marked in red in the respective figures. As depicted in Fig. 6(c), during tensile preload unloading and the initial elastic shear load along the perpendicular axis, the value of $\bar{\theta}_a$ quickly increases to one, while the equivalent plastic strain $\bar{\gamma}$ remains constant. In the subsequent shear loading stage, the $\bar{\theta}_a$ value decreases until it reaches approximately 0.08. A similar tendency is observed in the non-proportional ST loading pattern, although the angle parameter does not approach zero before the fracture point (FP) and continues to decrease in this case. In addition, the non-proportionality parameter $\bar{\theta}_b$ decreases from 1 to 0.5 as the mean equivalent plastic strain $\bar{\gamma}$ increases from 0.08 to 0.13 in the mon-TS test. In contrast, it decreases more slowly in the mon-ST test, with the same drop to 0.5 occurring over an equivalent plastic strain range $\bar{\gamma}$ from 0.24 to 0.33. These findings indicate that the change in loading direction between tension and shear is successfully characterized.

4.3. Strain hardening under non-proportional loading

The non-proportional experiment mon-TS, taken from the literature (Brünig et al., 2021), and the newly designed shear-tension cyclic loading tests cyc-TS-T0.05S0.1 and cyc-ST-S0.25T0.1 are shown in Fig. 7 to illustrate the non-proportional hardening effect. As shown in Fig. 7(a), the numerical result using the Brünig model (Brünig et al., 2021), which considers only isotropic hardening and does not include the strain hardening under non-proportional loading, agrees well with the experimental data overall but fails to accurately predict the hardening behavior at the beginning of the shear loading, where non-proportionality parameter $\bar{\theta}_b$ (Fig. 6(c)) is greater than 0.5. In contrast, the numerically predicted load–displacement curve using the proposed model significantly improves the accuracy. A similar result can be observed in the cyc-TS-T0.05S0.1 test, where the proposed model provides a better

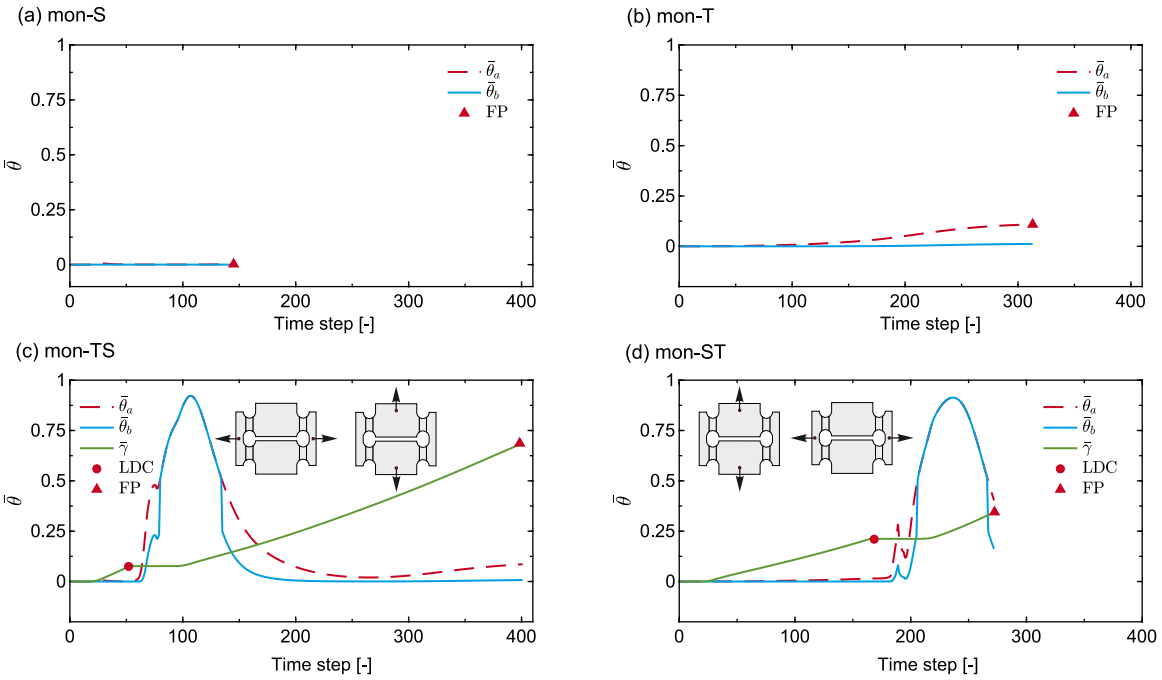

Fig. 6. The respective angle parameters $\bar{\theta}_a$ and $\bar{\theta}_b$ as well as the mean equivalent plastic strain $\bar{\gamma}$ versus time step. LDC refers to the loading direction change point, and FP denotes the fracture point.

characterization of the shear loading response due to its consideration of strain hardening under non-proportional loading, as shown in Fig. 6(b). A detailed comparison of the experimentally measured and numerically predicted load–displacement curves for axis 1 and axis 2 is shown in Fig. 6(b1) and (b2), respectively. Moreover, in the loading pattern cyc-ST-S0.25T0.1, which corresponds to a shear-to-tension-based non-reverse cyclic pattern, both the currently proposed combined hardening model and the Brünig isotropic hardening model can capture the load–displacement curve in the shear loading direction, as evidenced by comparison with the experimental results shown by the solid line in Fig. 7(d). However, the numerical results obtained from the Brünig model, which incorporates only isotropic hardening, overestimate the experimental data compared to the proposed model. This highlights that the combined hardening model offers a more accurate representation of the material response under non-proportional loading.

Furthermore, Fig. 7(c1) and (c2) illustrate a comparison between the experimental results and the respective numerical predictions for the loading path cyc-TS-T0.05S0.1, obtained using the combined hardening model without considering strain hardening under non-proportional loading (Wei et al., 2023b) and the currently proposed model. A significant improvement in numerical accuracy is observed for both shear and tensile loading patterns. It is clear that incorporating strain hardening under non-proportional loading based on the non-proportionality parameter $\bar{\theta}_b$ is necessary to enhance the previous combined hardening model (Wei et al., 2023b). Thus, in this paper, only the numerical results using the current proposed material model are discussed in the following sections, as the limitations of previous models have been demonstrated in characterizing the material behavior under non-proportional shear-tension cyclic loading conditions.

5. Results

5.1. Global load–displacement curves and local strain fields

A comparison of the experimental and numerical load–displacement curves for monotonic tensile and shear loading is shown in Fig. 8(a) and (b). The results clearly demonstrate the modeling accuracy under both monotonic and proportional loading conditions. Moreover, the experimental and numerical load–displacement curves for the non-proportional tension-to-shear (TS) and shear-to-tension (ST) cyclic loading patterns are shown in Figs. 9 and 10, respectively. It is evident that all numerical results show good agreement with the experimental ones. In addition, the displacements and forces at the fracture points, $\Delta u^{\mathrm{fr}}_{\mathrm{ref},2}$ and F^{fr}_2, and at the end of the last shear loading pattern, $\Delta u^{\mathrm{end}}_{\mathrm{ref},1}$ and F^{end}_1, are summarized in Table 4. N denotes the cycle number, where one full cyclic loading pattern is defined as tension (shear) loading followed by unloading and then shear (tension) loading followed by unloading. As observed in the experiments, all cyclic tests fail during the tensile loading path. Moreover, for the loading patterns cyc-TS, the cycle number is $N = 5$ when the displacement increment is $\Delta u^{\mathrm{M}}_2 = 0.05\,\mathrm{mm}$ (T0.05), and $N = 3$ when it is $\Delta u^{\mathrm{M}}_2 = 0.1\,\mathrm{mm}$ (T0.1). A similar tendency can also be observed in the cyclic experiments with ST loading patterns. The results indicate that tensile loading

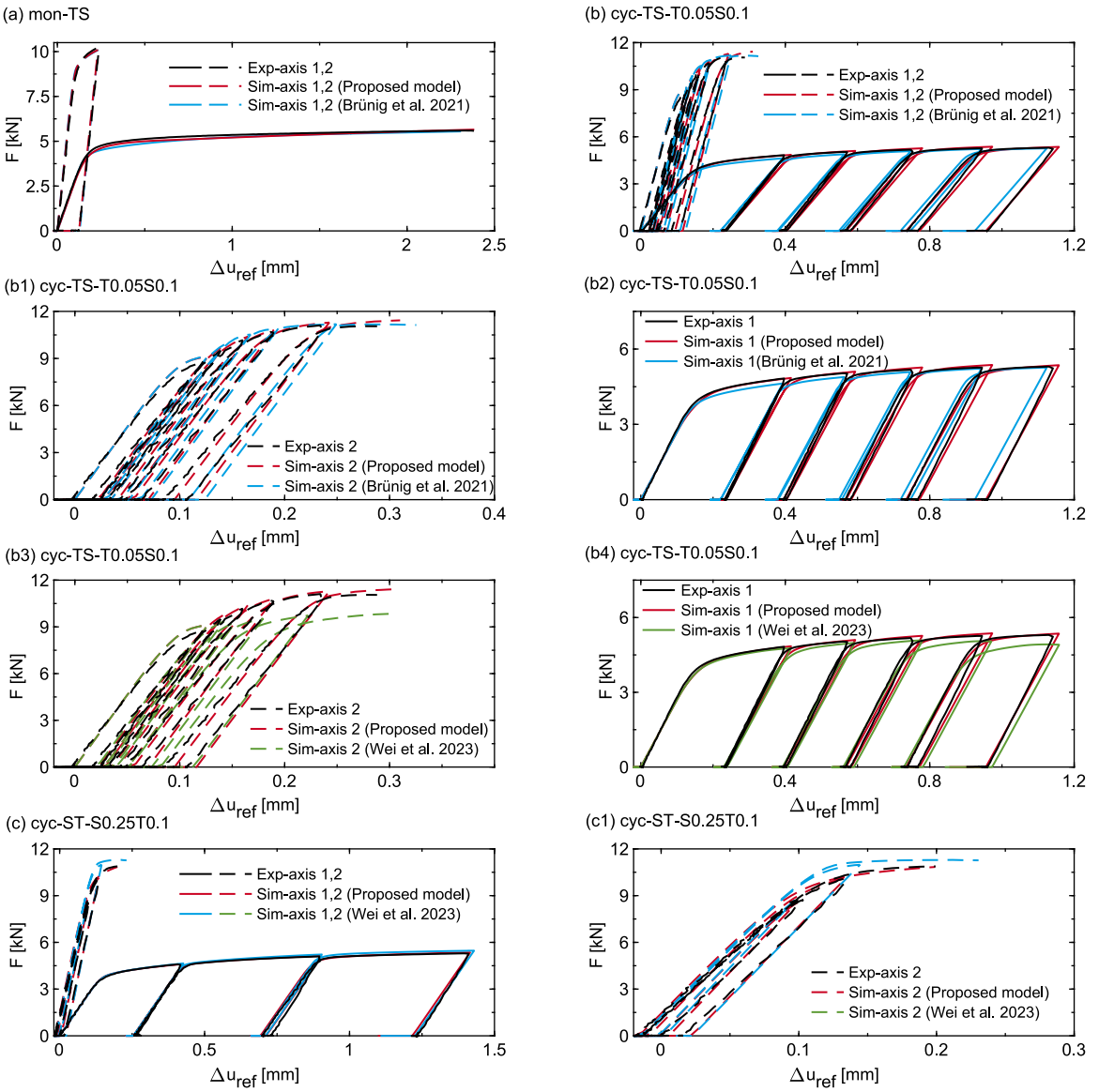

Fig. 7. Comparison of the experimental load–displacement curves for non-proportional monotonic and shear–tension cyclic loading with numerical predictions obtained using the current proposed model, an isotropic hardening model without considering the non-proportionality parameter (Brünig et al., 2021), and a combined hardening model without the non-proportionality parameter (Wei et al., 2023b). It is noted that the experimental data for the monotonic shear-tension (mon-ST) test is taken from the literature (Brünig et al., 2021).

Table 4
Experimentally measured forces and displacements at respective last tensile or shear loading patterns.

Tests	N [–]	$\Delta u_{ref,1}^{end}$ [mm]	$\Delta u_{ref,2}^{fr}$ [mm]	F_1^{end} [kN]	F_2^{fr} [kN]	Tests	N [–]	$\Delta u_{ref,1}^{end}$ [mm]	$\Delta u_{ref,2}^{fr}$ [mm]	F_1^{end} [kN]	F_2^{fr} [kN]
mon-T	0	−0.03	0.45	−0.04	10.41	mon-S	0	2.49	−0.23	5.56	0
cyc-TS-T0.05S0	5	0.45	0.36	4.57	10.85	cyc-ST-S0.15T0.05	4	1.46	0.23	5.27	10.76
cyc-TS-T0.05S0.1	5	1.13	0.29	5.30	11.05	cyc-ST-S0.15T0.1	3	1.22	0.27	5.25	10.89
cyc-TS-T0.05S0.15	5	1.51	0.21	5.51	11.23	cyc-ST-S0.25T0.1	3	1.41	0.21	5.27	10.88
cyc-TS-T0.1S0	3	0.41	0.36	4.53	10.59						
cyc-TS-T0.1S0.1	3	0.76	0.27	5.03	11.48						
cyc-TS-T0.1S0.15	3	0.93	0.31	5.27	11.05						

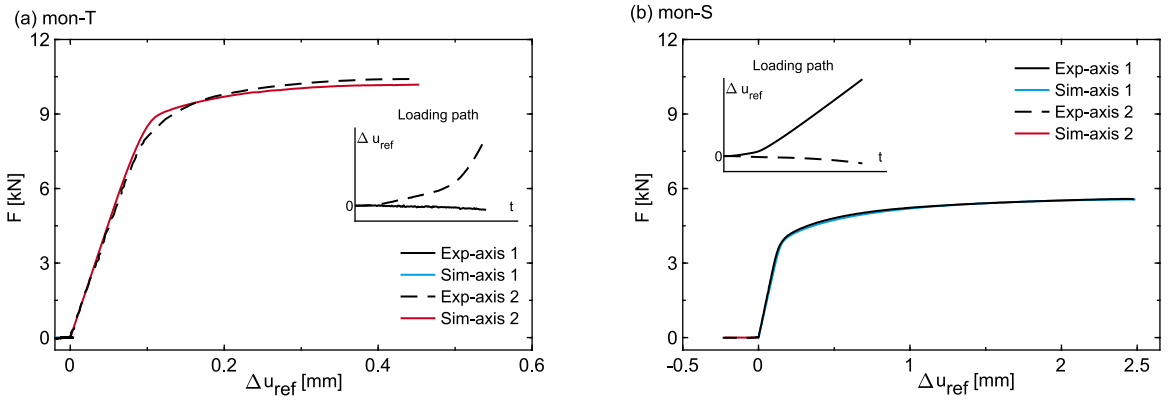

Fig. 8. Experimentally measured and numerically predicted load—displacement curves for the monotonic tensile test (a) and monotonic shear loading (b). Note that the u_{ref}–t plots at the top right of each subfigure show the experimentally measured relative displacement between the gauge points (see Fig. 2(e)) along different axes versus time.

patterns play a dominant role in the final fracture behavior, and the corresponding displacement increments determine the number of loading cycles.

By comparing the fracture forces, it can be seen that the cyclic loading patterns generally result in greater fracture forces F_2^{fr} than those under monotonic tensile loading conditions (mon-T). In the case of the cyclic loading pattern cyc-TS, experiments with a displacement increment $\Delta u_1^{\text{M}} = 0$ (S0) consistently show the lowest fracture forces F_2^{fr} among all loading cases with the same tensile displacement increment Δu_2^{M}. This reveals that the shear loading pattern contributes to increased strain hardening, resulting in higher fracture forces. On the other hand, the fracture forces F_2^{fr} for the loading case cyc-ST differ only slightly. Moreover, the fracture forces for the experiments cyc-ST-S0.15T0.05 and cyc-ST-S0.15T0.1 are smaller compared to the respective loading patterns cyc-TS-T0.05S0.15 and cyc-TS-T0.1S0.15. As designed, the experiments cyc-ST-S0.15T0.05 and cyc-TS-T0.05S0.15, as well as cyc-ST-S0.15T0.1 and cyc-TS-T0.1S0.15, have the same displacement increments in the respective axes, but differ in loading sequence. These findings clearly indicate that the loading sequence affects the material behavior at the macroscopic level.

A contour plot of the experimentally measured first principal logarithmic strains A_1 on the notch surface before the fracture points, along with the respective numerically predicted values, is depicted in Fig. 11. To quantitatively compare the values of the first principal strains A_1 throughout the entire loading patterns, the same region of interest (ROI), $0.5\,\text{mm} \times 0.25\,\text{mm}$, is defined at the center of the notch surface. The mean values over this area are illustrated in Fig. 12. One can observe that all numerical results align well with the experimental ones throughout the loading process as well as at the fracture points. As shown in Fig. 11(i), an elliptical strain distribution can be observed, with a maximum principal strain of $A_1 = 0.13$ for the mon-T test. For both the mon-S and cyclic loading patterns, a shear band appears on the notch surface. Among them, the mon-S case exhibits the maximum principal strain value of $A_1 = 0.63$ and shows evident deformation at the top-right and bottom-left edges of the notch. On the other hand, the cyclic loading pattern with a displacement increment $\Delta u_1^{\text{M}} = 0$ (S0) in the shear loading direction shows a shear band oriented along the northwest direction (from top left to bottom right), which differs from the other cyclic loading patterns where the band is oriented toward the northeast. Additionally, the width of the shear band is significantly greater than in the other cyclic loading patterns, as illustrated in Fig. 11(a) and (d). Moreover, both the angle between the shear band and the vertical symmetric axis, as well as the maximum value of the principal strain A_1, increase in experiments with the same machine displacement increment in the tensile direction Δu_2^{M}, as the displacement increment Δu_1^{M} in the shear loading direction increases. As observed in Table 4, the cyclic loading patterns cyc-TS-T0.05S0.15 and cyc-ST-S0.15T0.05 result in significantly greater shear deformations $\Delta u_{\text{ref},1}^{\text{end}}$, leading to the highest maximum principal strain values of approximately $A_1 = 0.35$ compared to those in other cyclic loading patterns. These observations highlight the influence of shear loading histories on the local distribution and maximum values of the strains.

Furthermore, the evolution of the first principal strain A_1 in the cyc-TS-T0.05S0 and cyc-TS-T0.1S0 experiments, shown in Fig. 12(c) and (d), reveals a significant increase from 0.01 to 0.05 during the first shear loading pattern. It is worth noting that both loading cases show the same strain values during the initial stage, as all cyclic loading patterns are subjected to the same displacement, as listed in Table 2. In addition, the final maximum value just before fracture reaches $A_1 = 0.10$, as shown in Fig. 11(a) and (d), indicating that shear band strains predominantly develop in this stage. Moreover, the values of the first principal strain A_1 increase more slowly during the tensile loading pattern than during the shear loading patterns, as shown in Fig. 12(g)–(h). The reason is that under tension-dominated stress states, strain localizes at the center of the notch interior, whereas under shear loading patterns, strain localizes in the form of a shear band on the notch surface. As a result, the maximum strain value under monotonic shear loading (mon-S) is significantly larger than that one observed under monotonic tensile loading (mon-T), see Figs. 11(i) and (j) and 12(a) and (b).

In addition, it can also be observed that the evolution tendency of the first principal strain A_1, as illustrated in Fig. 12(e)–(g), are quite similar for the cyclic experiments with the same machine displacement in the tensile loading direction Δu_2^{M}. However, the resulting maximum values of A_1 just before fracture differ due to the different imposed shear deformations. In addition, for a given

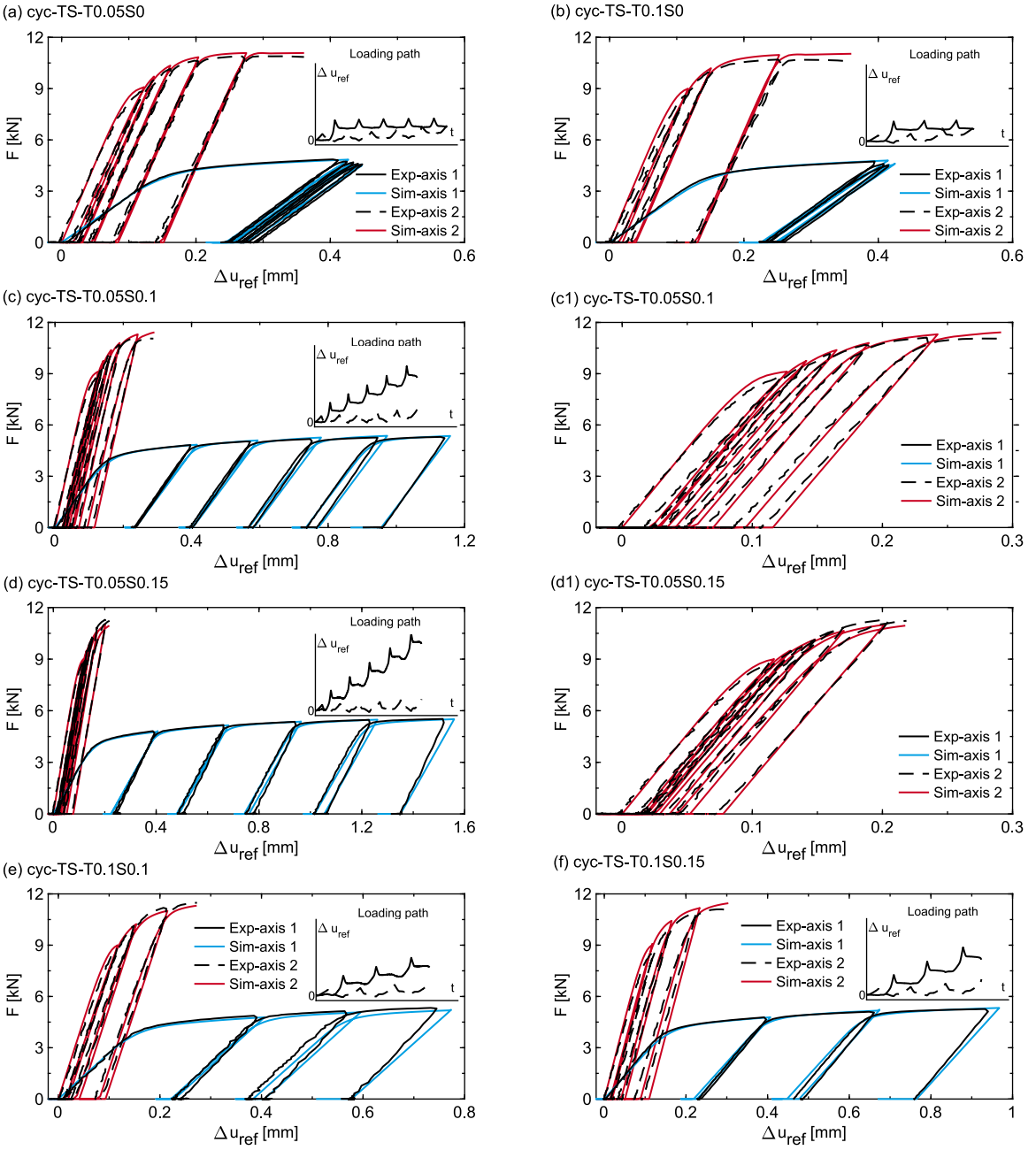

Fig. 9. Experimentally measured and numerically predicted load–displacement curves for non-proportional tension-to-shear (TS) cyclic loadings. Subfigures (c1)–(d1) additionally show the respective experimental and numerical results for axis 2. Note that the u_{ref}–t plots at the top right of each subfigure show the experimentally measured relative displacement between the gauge points (see Fig. 2(e)) in different axes versus time loading paths.

machine displacement increment in the shear loading direction Δu_1^{M}, a larger machine displacement increment in the tensile direction Δu_2^{M} leads to higher strain values. For example, at the same relative displacement along the shear loading axis $\Delta u_{\mathrm{ref},1} = 0.77\,\mathrm{mm}$, the first principal strains for tests cyc-TS-T0.05S0.1 and cyc-TS-T0.1S0.1 are $A_1 = 0.125$ and $A_1 = 0.136$, respectively. Similarly, for tests cyc-TS-T0.05S0.15 and cyc-TS-T0.1S0.15, the respective values are $A_1 = 0.235$ and $A_1 = 0.270$. These strain values increase only slightly during the respective pre-tensile loading pattern, as a nearly constant trend is observed in Fig. 12(e) and (f). This may indicate that, due to the change in loading direction, different magnitudes of tensile loading affect the non-proportional strain hardening during the subsequent shear loading stages. On the other hand, for a given machine displacement increment in the tensile direction Δu_2^{M}, the first principal strain A_1 increases slightly with increasing shear displacement in the cyclic loading tests.

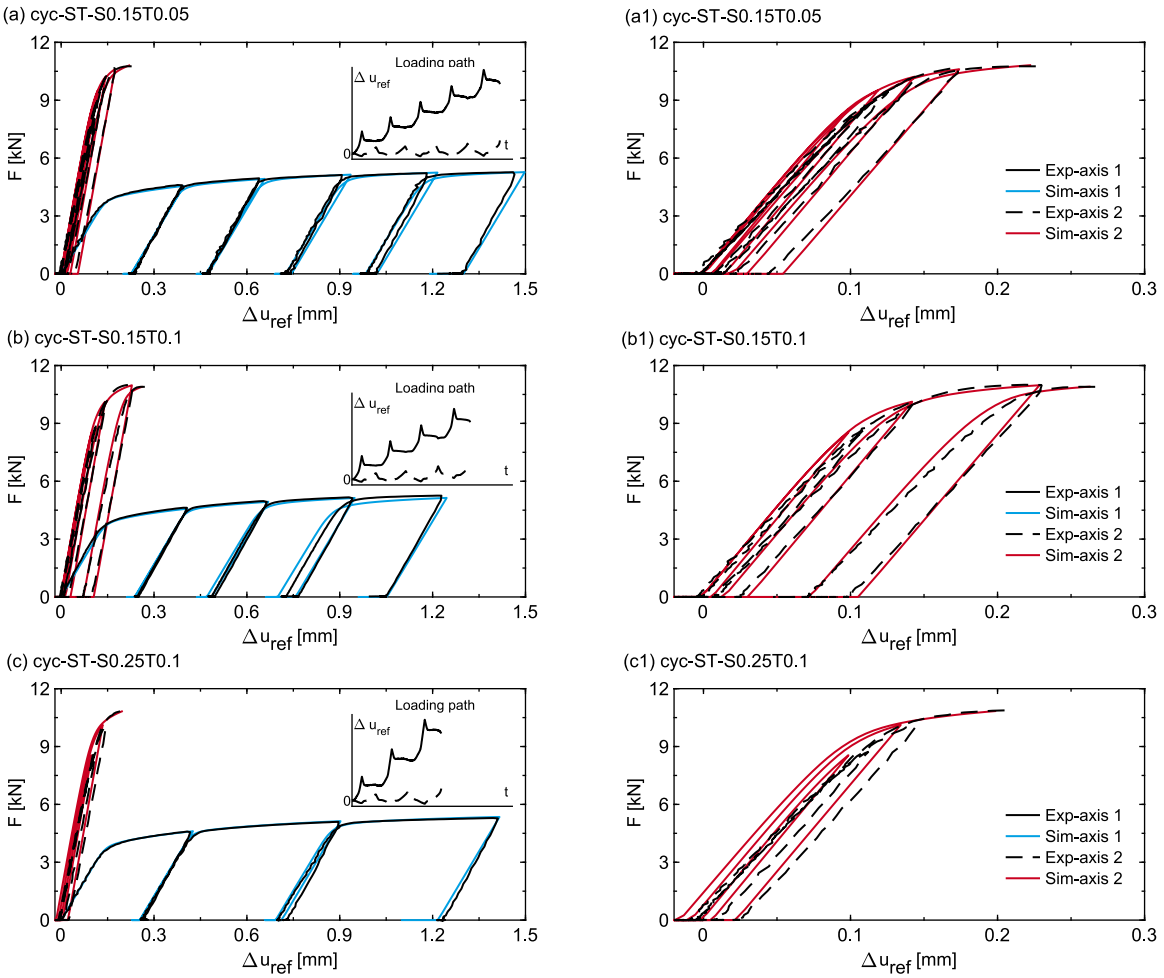

Fig. 10. Experimentally measured and numerically predicted load–displacement curves for non-proportional shear-to-tension (ST) cyclic loadings are shown in subfigures (a)–(c). The corresponding experimental and numerical results for axis 2 are additionally presented in subfigures (a1)–(c1). Note that the u_{ref}–t plots at the top right of each subfigure show the experimentally measured relative displacement between the gauge points (see Fig. 2(e)) in different axes versus time loading paths.

As observed, the strain increments ΔA_1 corresponding to a shear displacement increment of $\Delta u_1^{\mathrm{M}} = 0.25\,\mathrm{mm}$ are $\Delta A_1 = 0.09$ and $\Delta A_1 = 0.12$ in the second and third loading sequences, respectively. These observations highlight how the loading sequence of tension-to-shear and shear-to-tension affects the development of strain histories. The maximum values of the first principal strains on the notch surface are mainly developed and formed during the shear loading patterns.

5.2. Stress states and damage analysis

For the proposed damage mechanics model, the occurrence and development of damage depend on the respective stress states. Therefore, it is essential to analyze the evolution of the stress state during the loading process. Since the stress states over the notch surface are generally homogeneous, noticeable gradients appear only at the edges of the cross-section.

Thus, a mean value $\bar{\eta}$, as defined in Eq. (27), is used over the notched cross-section to quantitatively capture the evolution of stress triaxiality under the designed experimental loading paths. The respective mean stress triaxialities versus the relative displacements are shown in Fig. 13. In the monotonic loading cases, the mean stress triaxialities for the mon-T and mon-S loading conditions are $\bar{\eta} = 0.69$ and $\bar{\eta} = 0.09$, respectively, at their corresponding fracture points. The mean stress triaxialities vary between approximately 0.6 and 0.1 under cyclic loading conditions, which is attributed to the non-proportional loading paths. In addition, it can be observed that the values of the mean stress triaxiality $\bar{\eta}$ are approximately 0.66 for the cyclic loading patterns without displacement increments in the shear loading direction (S0), such as cyc-TS-T0.05S0 and cyc-TS-T0.1S0, whereas $\bar{\eta} = 0.6$ is obtained for the other cyclic loading patterns. This indicates that the shear loading patterns influence the stress states during the loading process. However, different increments of shear deformation do not significantly affect the stress states.

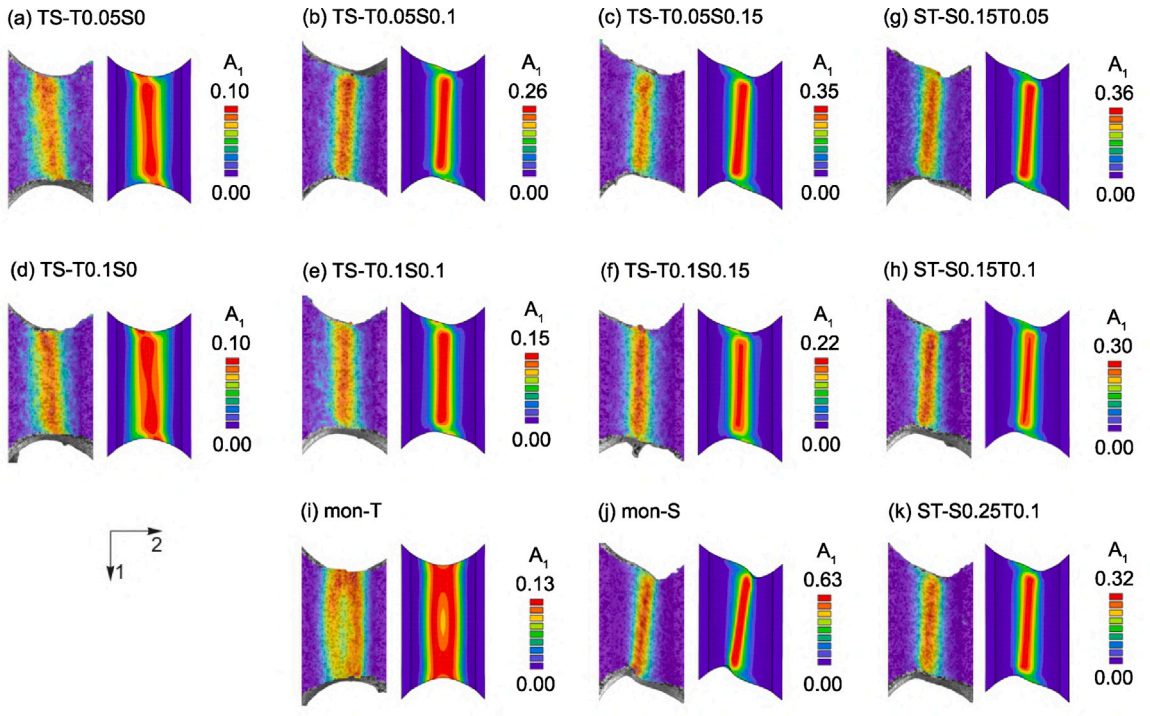

Fig. 11. Experimentally measured (DIC,left) and numerically predicted (right) first principal logarithmic strains A_1 on the notch surfaces (1-2 plane). The coordinate system 1-2-3 is illustrated in Fig. 5.

Moreover, the numerically predicted first principal damage strain A_1^{da} is plotted on different surfaces as shown in Fig. 14. Under monotonic loading conditions, the maximum values of A_1^{da} occur at different locations. In the mon-T test, the maximum value of A_1^{da} reaches 6.71% at the center of the notched cross-section, see Fig. 14(i). In contrast, for the mon-S test in Fig. 14(j), the maximum value of $A_1^{\mathrm{da}} = 0.77\%$ appears on the notch surface near the top and bottom edges, where significant deformation is observed. In the case of cyclic loading without progressive displacement increment in the shear loading direction (S0), damage is numerically predicted only at the center of the notch cross-section. The respective maximum values are 2.95% and 2.57% for the cyc-TS-T0.05S0 and cyc-TS-T0.1S0 tests, showing a similar damage strain distribution to that observed in the mon-T test, as illustrated in Fig. 14(i). However, their maximum values are significantly smaller than those observed in the mon-T experiment, even though the stress state at the fracture points differs slightly, with a difference of approximately 4%, as shown in Fig. 13. This indicates that although the shear loading following the tensile loading is relatively small, it still influences the damage development.

For the cyclic loading patterns with a machine displacement increment $\Delta u_2^{\mathrm{M}} = 0.05\,\mathrm{mm}$ (T0.05), namely TS-T0.05S0.1 in Fig. 14(b), TS-T0.05S0.15 in Fig. 14(c), and ST-S0.15T0.05 in Fig. 14(g), the maximum values of the damage strain are observed on the notch surface (1–2 plane) and the side surface of the notch (2–3 plane). As shown in Table 4, the corresponding shear displacements are $\Delta u_{\mathrm{ref},1} = 1.51\,\mathrm{mm}$ for TS-T0.05S0.15 and $1.46\,\mathrm{mm}$ for ST-S0.15T0.05, both noticeably higher than $\Delta u_{\mathrm{ref},1} = 1.13\,\mathrm{mm}$ for TS-T0.05S0.1, resulting in damage distributions that more closely resemble those observed in the mon-S test. On the other hand, for experiments with a machine displacement increment $\Delta u_2^{\mathrm{M}} = 0.10\,\mathrm{mm}$ (T0.10), the maximum damage is numerically observed in the notched cross-section (1–3 plane), as shown in Fig. 14(e), (f), (h), and (k), similar to the distribution observed in the mon-T test in Fig. 14(i). However, noticeable differences are observed in the maximum values of A_1^{da}. One can observe that the maximum value on the notch surface increases with increasing shear displacement $\Delta u_{\mathrm{ref},1}$, as discussed in Table 4. By comparing the damage distribution and magnitude between the experiments cyc-TS-T0.05S0.15 and the cyc-ST-S0.15T0.05 in Fig. 14(c) and (g), the change in the sequence of tension and shear loading shows no significant difference. However, a slight difference is observed between the loading patterns cyc-TS-T0.1S0.15 and cyc-ST-S0.15T0.1, as illustrated in Fig. 14(f) and (h). The above-mentioned analysis of the damage strain distributions and their maximum values reveals the influence of loading sequence and history on the damage behavior. Although the stress states at the final loading stage are all high, with stress triaxialities exceeding 0.6, different displacement increments in the various loading patterns result in different critical damage locations, either on the notch surface, within the notched cross-sections, or along the edge surfaces of the notch.

5.3. Fracture surfaces and SEM images

Fig. 15 shows a representative SEM image of the fracture subsurface (1–3 plane) and the fracture line on the notch surface (1–2 plane). The SEM images were taken from the notched cross-sections. As an example, a representative SEM image in Fig. 15(a) was

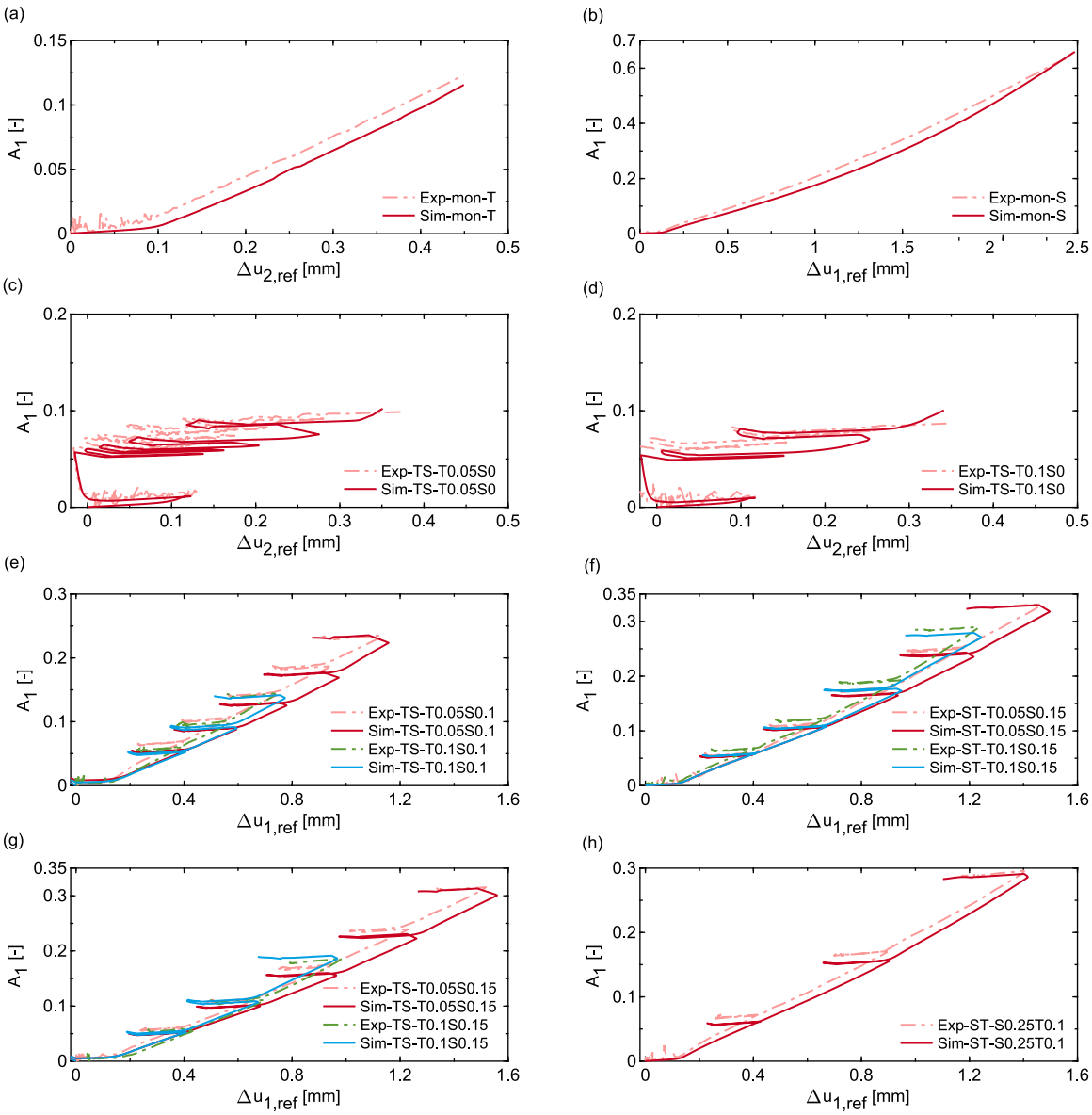

Fig. 12. Experimentally measured and numerically predicted evolution of the first principal strains A_1 in the region of interests (ROI) on the surface during the loading processes.

taken from the fractured notch cross-section illustrated in Fig. 15(a1). Note that for every fractured notch surface, three images were taken from the left, middle, and right regions to more accurately characterize the surface behavior. The fracture line under shear monotonic loading (mon-S) is significantly smoother and straighter compared to other loading conditions, where uneven fracture lines typically occur due to tensile-dominated fracture mechanisms, as seen in the cup-cone fracture surfaces observed in the uniaxial tension test (Wei et al., 2022). In addition, the angle between the fracture line and the vertical symmetry axis increases with the increasing shear deformation during the cyclic loading patterns, which is consistent with the observed distribution of the shear band in the first principal strain plots shown in Fig. 11.

Among the SEM images, Fig. 15(b) differs from the others, as it reveals micro-shear-cracks caused by a shear-dominated damage mechanism. In contrast, the other images predominantly show damage resulting from the growth and coalescence of micro-defects. This confirms that the low-stress states observed in the mon-S experiment, characterized by stress triaxialities close to zero, are associated with shear-dominated damage mechanisms, whereas high-stress states correspond to tension-dominated conditions. In addition, larger coalesced and shear-deformed micro-defects can be observed under cyclic loading conditions with a nonzero shear displacement increment, compared to monotonic tensile loading (mon-T) and cyclic loading with zero shear displacement increment (S0). This may be due to the continued shear deformation of previously formed micro-defects during the shear loading patterns.

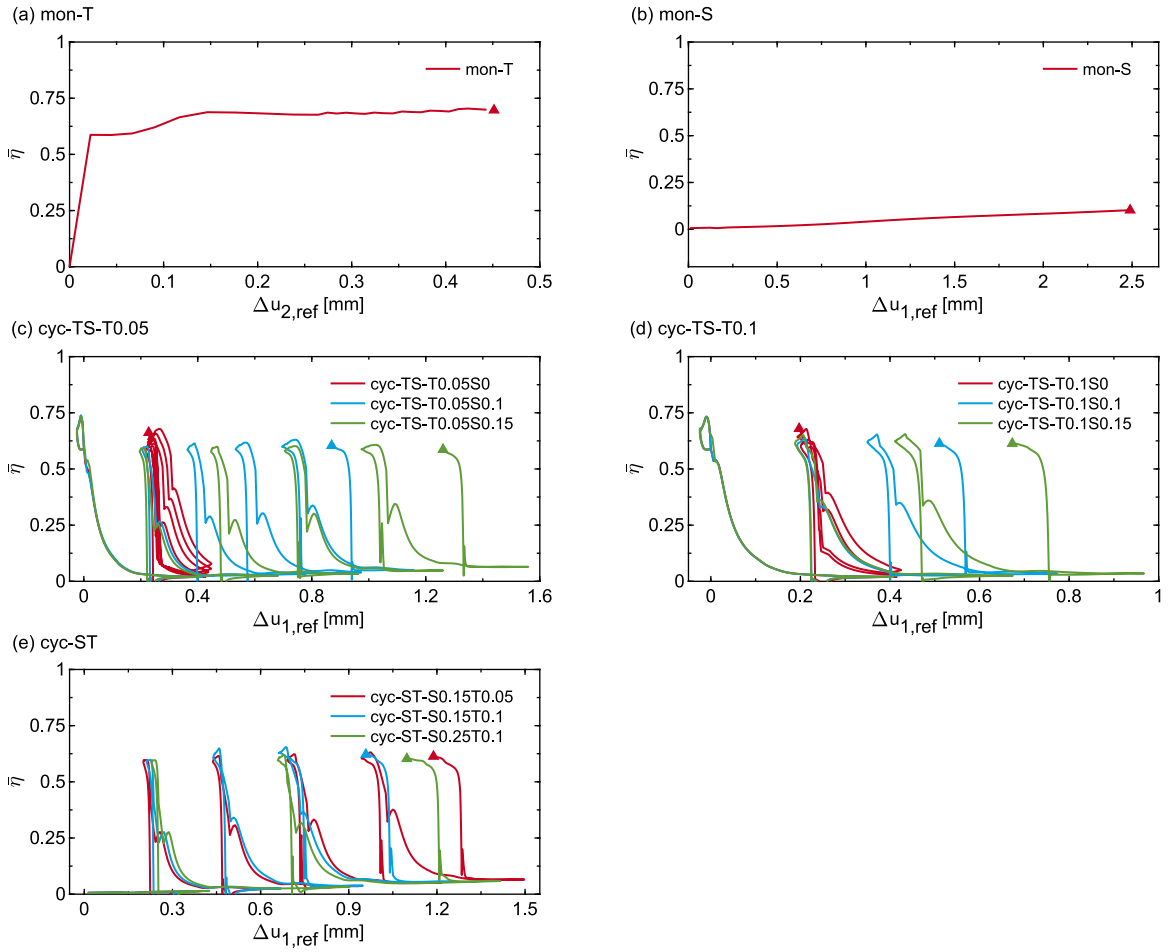

Fig. 13. Numerically predicted mean stress triaxialities $\bar{\eta}$ on the notched cross-section versus the respective relative displacements $\Delta u_{1,\mathrm{ref}}$ and $\Delta u_{2,\mathrm{ref}}$.

For the accurate analysis of SEM images, a machine learning approach is introduced in this work to characterize micro-defect behavior. Although traditional techniques using the Otsu threshold algorithm (Otsu, 1979) automatically produce results, they tend to overestimate the overall porosity due to difficulties in accurately distinguishing grayscale levels. While better results can be achieved through manual adjustment, this process is time-consuming and significantly slower than the fully automated CNN-based approach. The research group has compiled a comprehensive dataset of SEM images of the investigated aluminum alloy subjected to various loading conditions, as documented in publications (Brünig et al., 2021; Wei et al., 2022; Zistl et al., 2022; Wei et al., 2023b,c, 2024a, 2025b). The convolutional neural network-based model, DeepLabv3, with the ResNet-50 backbone, a branch of artificial neural networks (ANN), is used for semantic segmentation. Implemented using an open-source deep learning framework (PyTorch), it is trained to classify different types of micro-voids. The model and training data are explicitly processed on the GPU to accelerate computation. Additionally, the key parameters for the training process are as follows: the batch size is set to 2, the total number of epochs is 200, the learning rate is set to 0.0001, and the Adam optimizer is employed. The original SEM images, taken under 100x magnification with a resolution of 3072 × 2304 pixels, are divided into several sub-images with a resolution of 480 × 480 pixels for manual annotation of micro-voids. The labeling process is conducted using the open-source software LabelMe. Each void region is manually annotated using polygonal shapes. The resulting annotations are transformed into binary masks and used together with the corresponding original images to train and validate the neural network. In total, 500 sub-images are generated, with 76% (380 sub-images) used for training and 24% (120 sub-images) reserved as a validation dataset. It should be noted that the present work involves semantic segmentation, where each image contains multiple voids of varying shapes and contrast, all of which must be identified at the pixel level. Therefore, although the dataset includes only 500 images, it contains numerous voids with diverse features, shapes, and contrast levels. Additionally, random data augmentation, such as horizontal and vertical flipping, enables the network to learn a broader range of features. In addition, training with 500, 700, and 900 images produced similar results, indicating that increasing the amount of data did not significantly affect the model's accuracy. The training performance indicates strong results, with training accuracy reaching 99.2% and validation accuracy reaching 92.7%. The precision, recall, and Dice scores

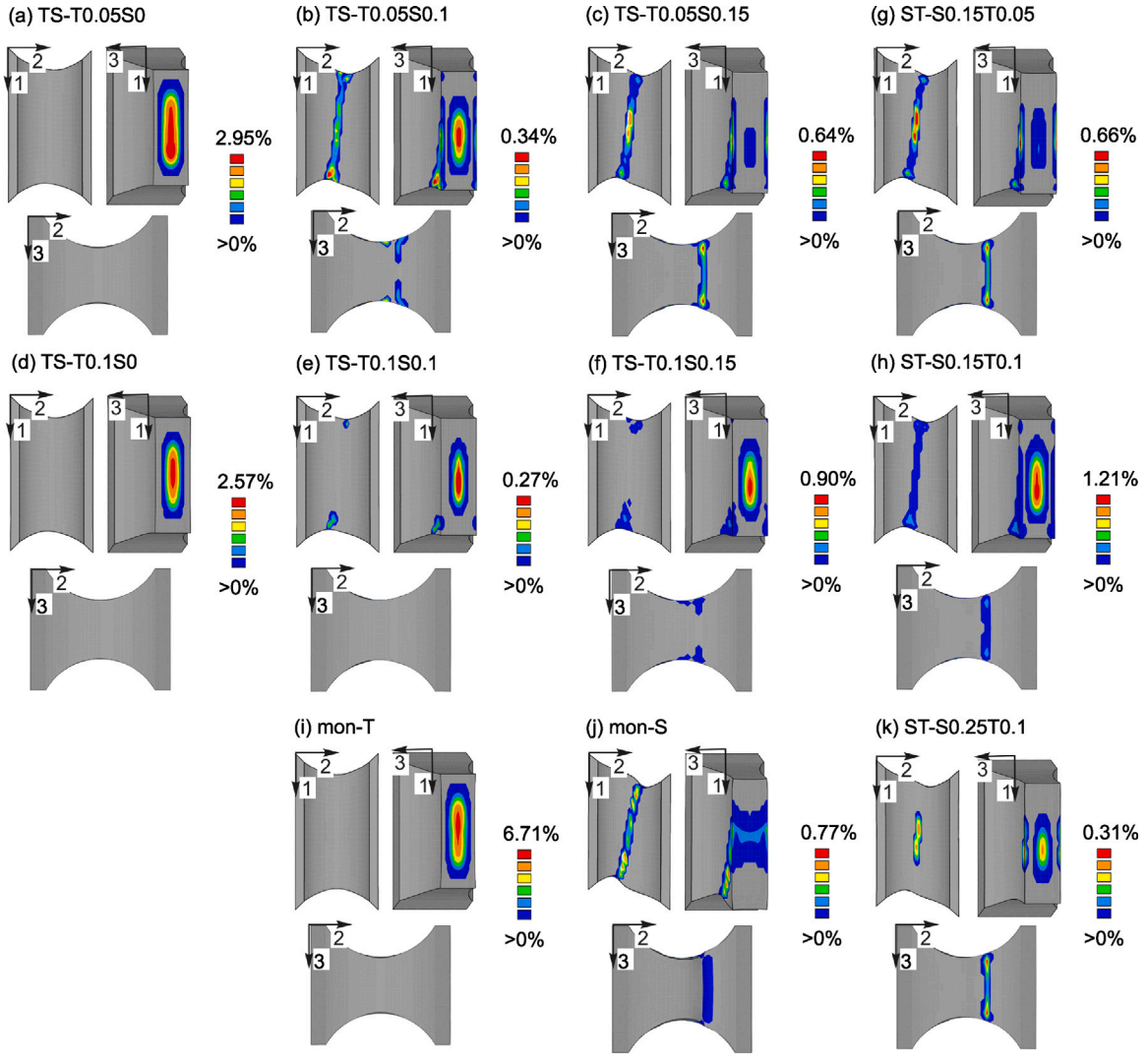

Fig. 14. Numerically predicted first principal damage strains A_1^{da} on the notch surfaces (1–2 plane), the notched cross-sections (1–3 plane), and the surfaces of the notch edge (2–3 plane). The coordinate system 1-2-3 is illustrated in Fig. 5. Note that the gray color represents regions where no damage is numerically predicted. (For interpretation of the references to color in this figure legend, the reader is referred to the web version of this article.)

were all approximately 89%, indicating very good training performance, especially considering that even experienced experts often find it challenging to distinguish voids in SEM images accurately.

Fig. 16 shows the original SEM images (a) and (b), along with the predicted micro-voids using the trained DeepLabv3 model and ImageJ with manually adjusted and default thresholds, shown in (a1)–(a3) and (b1)–(b3). The micro-voids shown in Fig. 16(a1) and (b1) are visualized as segmentation masks recognized by the machine learning method and overlaid on the SEM images to enable qualitative evaluation of the fracture surface characteristics. It can be observed that the trained model effectively identifies micro-voids, and the porosities identified by the machine learning model for loading cases cyc-TS-T0.05S0 (Fig. 16(a)) and mon-S (Fig. 16(b)) are 48.12% and 1.71%, respectively. Compared to the machine learning method, the micro-void areas segmented by ImageJ, as shown in Fig. 16(a3) and (b3), using the default threshold, are significantly larger than those from the machine learning method, with respective porosities of 64.27% and 62.89%. This is clearly an incorrect prediction, especially in Fig. 16(b3), since only very few micro-voids can be observed in the original SEM image under the monotonic shear loading condition (mon-S), as illustrated in Fig. 16(b). After several time-consuming and challenging threshold adjustments using the ImageJ identification method, the obtained porosity values aligned with the machine learning values, with respective values of 46.34% for Fig. 16(a2) and 1.7% for Fig. 16(b2). Although the porosity in Fig. 16(a2), obtained through manual adjustment, is similar to that from the machine learning method, the uniform grayscale variation makes it challenging to identify the shape of the voids using thresholding accurately. This imprecision limits the analysis of void morphological features. Moreover, as shown in Fig. 16(b2), the lower right corner exhibits inaccurate

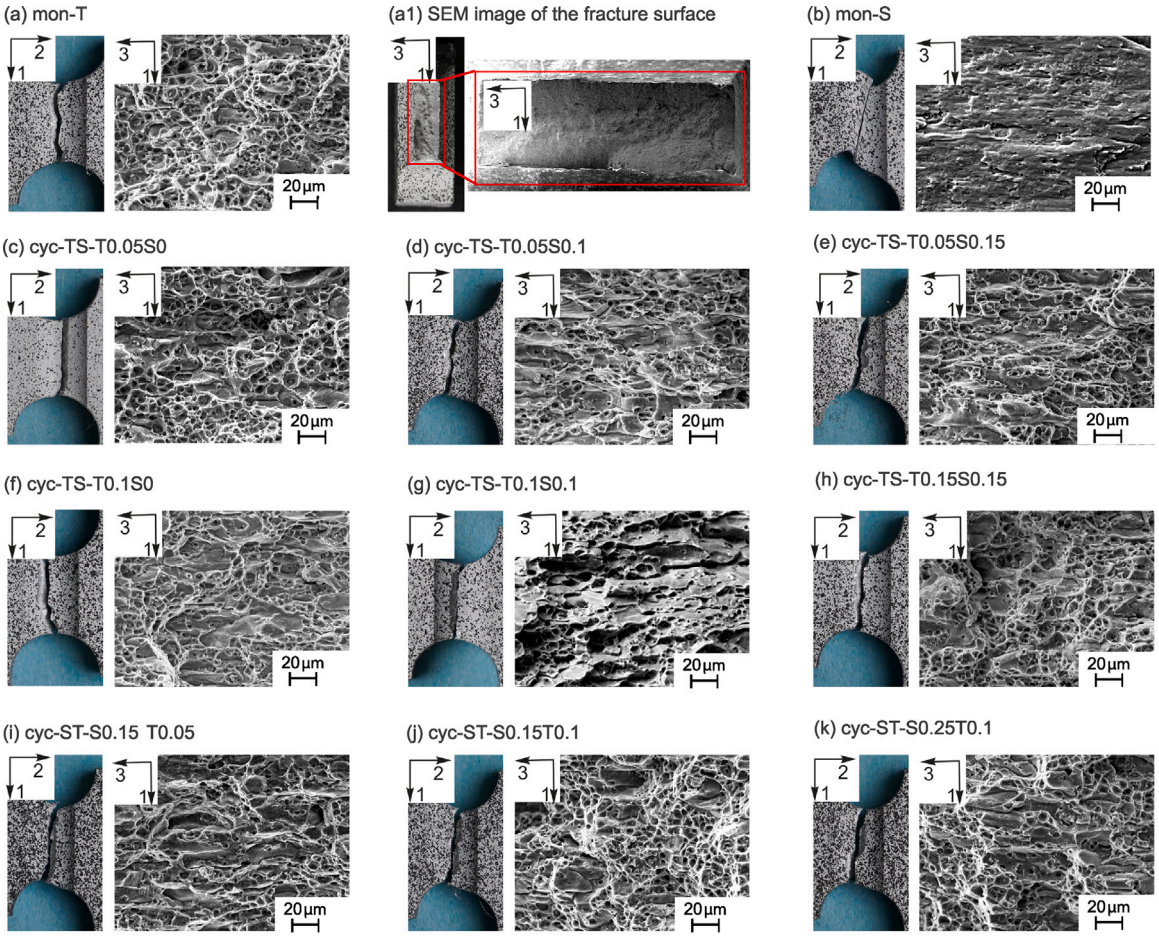

Fig. 15. SEM images of the fracture surfaces (1–3 plane) and fracture lines on the notch surface (1–2 plane). The coordinate system 1-2-3 is illustrated in Fig. 5.

segmentation due to a pronounced light–dark transition. These findings highlight the superior accuracy of the machine learning approach.

Moreover, the analysis of the SEM images is summarized in Table 5. It should be mentioned that, as noted in Section 2, three images were taken for each fracture surface; thus, all values presented in Table 5 are mean values. The micro-void fraction $\bar{f}$ for the mon-S experiment is significantly smaller than that of the other loading conditions, with a value of 2.20%. In addition, the micro-void size $\bar{s}$ is only 3.17 μm^2, which is 12% of the size measured under the mon-T test. This is consistent with the numerically predicted stress state of $\bar{\eta} = 0.1$, as shown in Fig. 13(b), which indicates a shear-dominated damage mechanism. In this case, the damage is caused by the growth and coalescence of micro-shear-cracks. The mean micro-void fraction $\bar{f}$ under cyclic loading patterns is clearly smaller than that observed under monotonic loading. Similarly, the mean micro-void area $\bar{s}$ in shear-to-tension cyclic loading cases (cyc-ST), as well as in the cyclic experiments with a progressive tensile loading increase characterized by a machine displacement of 0.1 mm (cyc-TS-T0.1), and in the loading cases cyc-TS-T0.05S0.1 and cyc-TS-T0.05S0.15, is smaller than in the monotonic test. This reduction results from the significantly greater shear deformation in these loading patterns, as summarized in Table 4, which leads to the slight closure of micro-voids and their elongation in the shear direction. On the other hand, the mean size $\bar{s}$ of the micro-voids for the tension-to-shear cyclic loading pattern cyc-TS-T0.05S0 with lower shear deformation is larger than that under monotonic loading. This indicates that the coalescence of micro-voids is significantly more pronounced in these cases compared to other cyclic loading patterns. These findings suggest that the loading and unloading processes, along with changes in loading direction that result in different shear loading histories, significantly influence the size, shape, and evolution of micro-defects.

Furthermore, different combinations of tensile and shear cyclic displacement increments result in distinct damage behaviors at the microscopic level. For example, when comparing different shear increments (S0.1 and S0.15) superimposed with respective tensile increments (T0.05 and T0.1), the resulting fracture displacements in both axis 1 and axis 2 differ, see Table 4. By comparing between cyc-TS-T0.05S0.1 and cyc-TS-T0.1S0.1, as well as between cyc-TS-T0.05S0.15 and cyc-TS-T0.1S0.15, a similar tendency can be observed: a larger tensile fracture displacement $\Delta u^{\mathrm{fr}}_{\mathrm{ref},2}$ is associated with a higher number of micro-voids, increased porosity, and a larger mean void area. This trend is also consistent with the numerically predicted maximum damage strain values. For

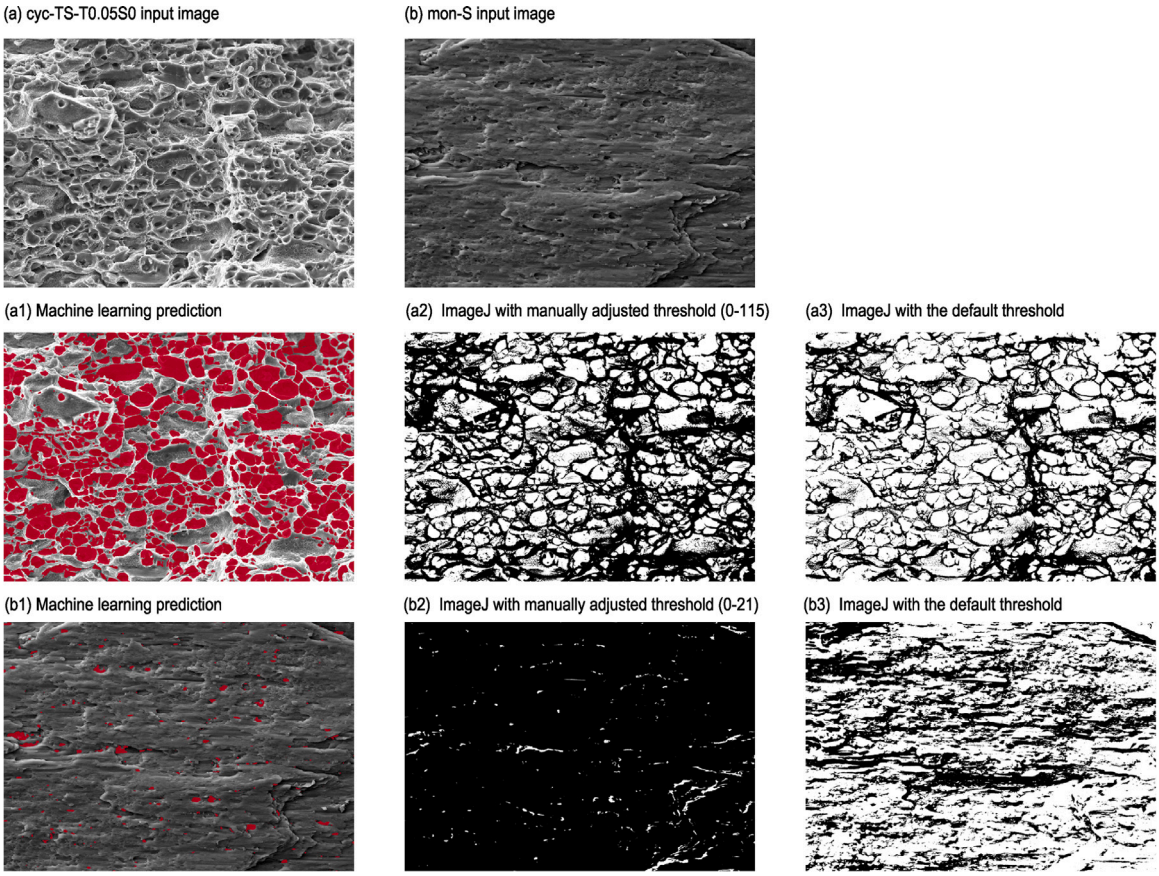

Fig. 16. Input SEM images (a) and (b) and a comparison of predicted segmentation masks showing classified micro-void regions using the trained DeepLabv3 model, ImageJ with manually adjusted and default threshold (a1)–(a3) and (b1)–(b3).

example, although the tensile displacement increment is smaller, the loading sequence cyc-TS-T0.05S0.1 results in a larger $\Delta u^{\mathrm{fr}}_{\mathrm{ref},2}$ than cyc-TS-T0.1S0.1. Accordingly, the characteristics of the micro-defects listed in Table 5, as well as the numerically predicted first principal damage strain values shown in Fig. 14, are also greater in cyc-TS-T0.05S0.1 than in cyc-TS-T0.1S0.1.

For the same combination of tensile and shear displacement increments with only different loading sequences, such as cyc-TS-T0.05S0.15 compared to cyc-ST-S0.15T0.05, and cyc-TS-T0.1S0.15 compared to cyc-ST-S0.15T0.1, both the void fraction and mean void size are smaller under TS loading patterns than under ST loading patterns. Also, the maximum numerically predicted first principal damage strain under the TS loading sequence is smaller than that under the ST loading sequence, as shown by the comparison in Fig. 14(c) and (g), as well as (f) and (h). Considering the fracture displacements along both axis 1 and axis 2, as presented in Table 4, the porosity and mean area of micro-voids are higher under the cyc-ST-S0.15T0.05 loading case than under cyc-TS-T0.05S0.15, which correlates with a slightly larger fracture tensile displacement $\Delta u^{\mathrm{fr}}_{\mathrm{ref},2}$. On the other hand, although the porosity under the cyc-ST-S0.15T0.1 loading sequence is comparable to that of cyc-TS-T0.1S0.15, the mean micro-void area remains nearly the same. Moreover, the total number of micro-voids is higher in the cyc-TS-T0.1S0.15 case, suggesting that the increase in porosity is mainly attributable to void nucleation rather than growth and coalescence. This may be attributed to the fact that previously formed micro-shear-cracks are more difficult to grow in the tensile direction after the loading direction changes from shear to tension, as also observed by Wei et al. (2023c, 2024a).

The above quantitative analysis of the micro-voids reveals a consistent pattern under different loading conditions, which aligns well with the overall trends observed in the globally measured fracture displacements and the numerically predicted damage strain values. These findings highlight that the machine learning approach can effectively capture microscopic micro-void characteristics and provide strong evidence to support and validate the proposed damage model at the microscopic level.

5.4. LOM analysis

Wei et al. (2024a) use light optical microscopy (LOM) to analyze the evolution of micro-defects (including micro-voids and micro-shear cracks) under cyclic loading tests with different complex loading conditions. The corresponding results quantitatively analyzed the evolution trend of micro-defects during cyclic loading. Following this success, LOM is used in the present study to

Table 5
Quantitative analysis of the mean number, void fraction, and mean size of micro-voids based on SEM images.

Test name	$\bar{N}_p$ [–]	$\bar{f}$ [%]	$\bar{s}$ [μm²]	Test name	$\bar{N}_p$ [–]	$\bar{f}$ [%]	$\bar{s}$ [μm²]	Test name	$\bar{N}_p$ [–]	$\bar{f}$ [%]	$\bar{s}$ [μm²]
mon-T	739	49.55	26.28					mon-S	264	2.20	3.17
cyc-TS-T0.05S0	584	48.92	33.50	cyc-TS-T0.1S0	869	42.13	19.61	cyc-ST-S0.15T0.05	741	39.46	20.71
cyc-TS-T0.05S0.1	702	38.78	21.38	cyc-TS-T0.1S0.1	583	28.49	18.87	cyc-ST-S0.15T0.1	819	41.49	19.84
cyc-TS-T0.05S0.15	726	30.99	17.00	cyc-TS-T0.1S0.15	755	37.89	19.45	cyc-ST-S0.25T0.1	768	42.44	21.45

characterize the different sizes of the specimen in various regions after fracture, as schematically indicated by positions N1 and N3 in Fig. 4. It is worth noting that the loading was applied continuously until the specimen failed, without interruption. Thus, the unfractured notch N3 might be due to geometric or material imperfections, and not all notches necessarily fractured during the experiments. The investigated aluminum samples are first cut from the specimens and then cold-mounted using an epoxy mixture with a weight ratio of 100 g of binder to 50 g of hardener. The curing process is conducted at room temperature in a fume hood for 24 h.

The goal of sample grinding is to expose the middle layer of the notch. As shown in Fig. 2, the original notch thickness is 2 mm, so grinding is performed until approximately 1 mm from the notch surface is reached. Sample grinding begins with the coarsest grit size of 120 to obtain an initially flat surface at the target position. To precisely capture the notch region of the manufactured samples, the first grinding step continues until about 0.4 mm away from the notch center, allowing for finer grinding and polishing. Progressive grinding is carried out using finer abrasive papers with grit sizes of 240, 320, 600, 1200, 2500, and 4000 to achieve a mirror-like surface. After grinding, the samples are manually polished using diamond slurries with particle sizes of 6, 3, and 1 μm to remove surface damage and deformation introduced during cutting, mounting, or grinding. It should be noted that etching was not used in the present work since the structures of the alloys are not of interest. The digital microscope VHX-7000, manufactured by Keyence, is used to analyze the samples. The automatic stitching function was configured to cover a 3 × 3 grid around the center of the notch at 100x magnification. The resulting image, taken at the center of the fracture and unfractured notch region, has a resolution of approximately 7065 × 5230 pixels. It should be noted that, due to the variety of surface characteristics, different image sizes were required for various areas to accurately capture the entire fractured notch edge. As an example, the LOM images of the fractured notches are illustrated in Fig. 17. It should be noted that the shown LOM images have been cropped from the original fracture notch images by approximately 50% to highlight the fracture lines better. The fracture edge in the mon-s experiment is significantly different from those observed under other loading conditions, exhibiting a nearly smooth edge in contrast to the more irregular, zigzag-like fracture edges seen in the others. To characterize the distribution of micro-defects near the edge and center of the fractured region, different LOM images were taken from these areas, referred to as the fractured edge and the fracture center, respectively, as shown in Fig. 4.

The open-source software ImageJ is used to analyze the mean area and area fraction of the micro-defects based on the light optical microscope images. The corresponding results are summarized in Table 6. For the analysis, the image is first converted to 8-bit format and then binarized to facilitate the capture of micro-defects. The scale is set to 0.96 pixel/μm. Micro-defect analysis is performed with a size range of 2–20 μm² and a circularity threshold of 0.50 to 1.00 to exclude non-particle (micro-defects) features such as suspensions or polishing-induced damage, as applied by Wei et al. (2024a) in the analysis of the same investigated aluminum alloy under cyclic loading to characterize the change of micro-defects. The undeformed material was taken from both the end of the axis and the notch area. It refers to the original, unloaded sample, directly cut from the manufactured specimen. The measured mean areas $\bar{s}$ are 5.321 μm² and 5.592 μm², respectively. The results show only a slight difference. For comparison, the value 5.592 μm² is used as the reference since all other measurements are taken from the notch area, and this choice helps to avoid potential errors caused by H-specimen manufacturing. It should be noted that the micro-defects observed in the LOM images are not conceptually the same as those observed in the SEM images. The micro-defects in LOM include both micro-voids (pores) and shear-deformed micro-voids (i.e., micro-shear-cracks). Therefore, the area fraction D measured in LOM does not represent the void fraction f show in Table 5.

By comparing the mean areas of the micro-defects in Table 6, it can be observed that the values near the fracture edge are significantly higher than those measured at the center of the fractured notch. Moreover, the values at the center of the fractured notch are greater than those at the center of the unfractured notch. While the values of the area fraction D measured at the fracture edge are smaller than those in the center of the fractured and unfractured notch regions, this suggests that the micro-defects near the notch edge are larger in size but fewer in number. This observation can be attributed to the coalescence of micro-defects resulting from high plastic deformation and strain localization in that region, ultimately leading to fracture. On the other hand, the mean area $\bar{s}$ measured at the center of both the fractured and unfractured notch regions is slightly smaller than that of the unfractured material, whereas the area fraction D is slightly higher compared to the reference values ($\bar{s} = 5.592$ μm² and $D = 2.114$). These observations suggest that the increase in the number of micro-defects during the loading process leads to the occurrence and development of damage. As observed in the mon-T and mon-S at the fracture edges, the values of $\bar{s}$ and D under monotonic tensile loading are both smaller than those under monotonic shear loading. It indicates that the size and number of micro-defects are greater under shear loading than under tensile loading. One possible reason is that under shear-dominated loading conditions, the existing micro-defects deform in the shear direction and more easily coalesce with neighboring micro-shear-cracks, leading to larger micro-defect areas. As also observed, for cyclic loading with a tension-to-shear pattern, increasing the shear deformation leads to larger mean areas. In

Table 6
The analysis of the mean area of the micro-defect (including micro-voids and micro-shear cracks) $\bar{s}$ and the area fraction D for the light optical microscope images.

Test name	Fractured edge (see N1 in Fig. 4)		Fractured center (see N1 in Fig. 4)		Unfractured center (see N3 in Fig. 4)	
	$\bar{s}$ [μm^2]	D [%]	$\bar{s}$ [μm^2]	D [%]	$\bar{s}$ [μm^2]	D [%]
Undeformed axis edge	n.a.	n.a.	n.a.	n.a.	5.321	2.257
Undeformed notch area	n.a.	n.a.	n.a.	n.a.	5.592	2.114
mon-T	5.518	1.731	5.253	2.549	5.205	2.180
mon-S	5.899	1.845	5.494	2.262	5.039	2.233
cyc-TS-T0.05S0	5.667	1.394	5.413	2.248	4.845	3.313
cyc-TS-T0.05S0.1	6.166	1.559	5.744	2.230	5.888	1.695
cyc-TS-T0.05S0.15	6.209	1.659	5.799	2.213	5.112	2.569
cyc-TS-T0.1S0	5.921	1.331	5.511	2.114	4.850	2.807
cyc-TS-T0.1S0.1	6.173	1.748	5.676	2.265	5.137	2.438
cyc-TS-T0.1S0.15	6.010	1.527	5.389	2.080	5.175	1.650
cyc-ST-S0.15T0.05	5.897	1.384	5.477	2.275	5.043	2.202
cyc-ST-S0.15T0.1	5.866	1.701	5.430	2.241	4.939	2.389
cyc-ST-S0.25T0.1	5.773	1.214	5.458	2.546	5.965	1.930

Note: It is worth noting that the loading was applied continuously until the specimen failed, without interruption. During the experiment, at least one notch remained unfractured, and the unfractured center region was selected from this area.

addition, the influence of the loading sequence also depends on different cyclic displacement increments. For example, the mean area of the micro-defects $\bar{s}$ for cyc-TS-T0.05S0.15 is larger than that in cyc-ST-S0.15T0.05, whereas the measured value shows only a negligible difference between cyc-TS-T0.1S0.15 and cyc-ST-S0.15T0.1. Moreover, the mean area of the micro-defects $\bar{s}$ is larger under cyclic loading than under monotonic loading, highlighting the increased coalescence of pre-existing micro-defects during cyclic loading patterns.

During the optical examination of the notch area, one crack is interestingly observed at the center of the unfractured notch under 100x magnification for the experiment cyc-TS-T0.05S0.1, as shown in Fig. 18. In addition, detailed views at 1000x and 2500x magnification are shown in Fig. 18(c) and (d), respectively, where it is evident that the crack extends through the specimen thickness and is caused by the loading process. This observation provides strong evidence that the crack initiation occurs at the notch center of the specimens. Moreover, the numerically predicted maximum value of the damage strain A_1^{da} also occurs at the center of the notch, consistent with the observation in the LOM image, as shown in Fig. 13. In addition, one can also observe that the distribution of micro-defects appears as a distorted wave pattern (marked by a red dashed line) in Fig. 18(b), with evident deformation at the edge of the notch, as illustrated in Fig. 18(a). This might be caused by the tension-to-shear cyclic loading, which results in strain localization and leads to crack formation. The absence of a final fracture may be due to crack tip blunting, which arrested or stabilized the damage evolution.

6. Conclusion

A novel set of non-proportional progressive and non-progressive cyclic experiments using 4 mm thick biaxially loaded H-specimens is designed and conducted to investigate ductile damage and fracture behavior at both macroscopic and microscopic levels. A key novelty of this study lies in the integration of non-proportional and cyclic loading concepts under large plastic strain amplitudes to study the initiation and evolution of ductile damage in thin metal sheets. Modern experimental techniques such as digital image correlation (DIC) are used to accurately capture the load–displacement response and strain fields, while scanning electron microscopy (SEM) and light optical microscopy (LOM) are employed to investigate the material behavior at the microscopic level.

For the material modeling part, a novel non-proportionality parameter is introduced within the combined hardening concept to capture the strain hardening induced by changes in loading directions during different cyclic loading patterns. The comparison between the previously proposed cyclic plastic-damage continuum model (Wei et al., 2023b) and the modified theory presented in this paper clearly demonstrates improved accuracy. The numerical results show very good agreement with the experimental data in terms of global load–displacement curves, local strain fields, and the evolution of strains during the experiments, demonstrating high accuracy.

Compared to the tension-to-shear cyclic loading pattern, the final fracture forces under shear-to-tension loading conditions are lower, and fracture occurs earlier, indicating a more brittle material behavior. All specimens subjected to cyclic loading failed during the final tensile loading pattern under similar tensile-dominated stress states, with an average stress triaxiality of 0.6. However, the damage and fracture behaviors differed, as predicted by numerical simulations and confirmed by quantitative analysis of SEM images of the fracture surfaces and LOM images of the middle layer at the center of both the fractured and unfractured notch regions, obtained from uninterrupted experiments. For the tension-to-shear (TS) loading with a tensile displacement increment of T0.05, the maximum damage strain exhibits a shear band distribution on the notch surface, indicating that the shear loading contributes more significantly to damage evolution compared to the TS cyclic loading with a larger tensile increment T0.1. For the TS loading with T0.1, the maximum damage is observed at the notch center, similar to the monotonic tensile loading or cyclic loading with zero shear displacement increment (S0). By comparing the global fracture tensile displacements and the numerically predicted maximum

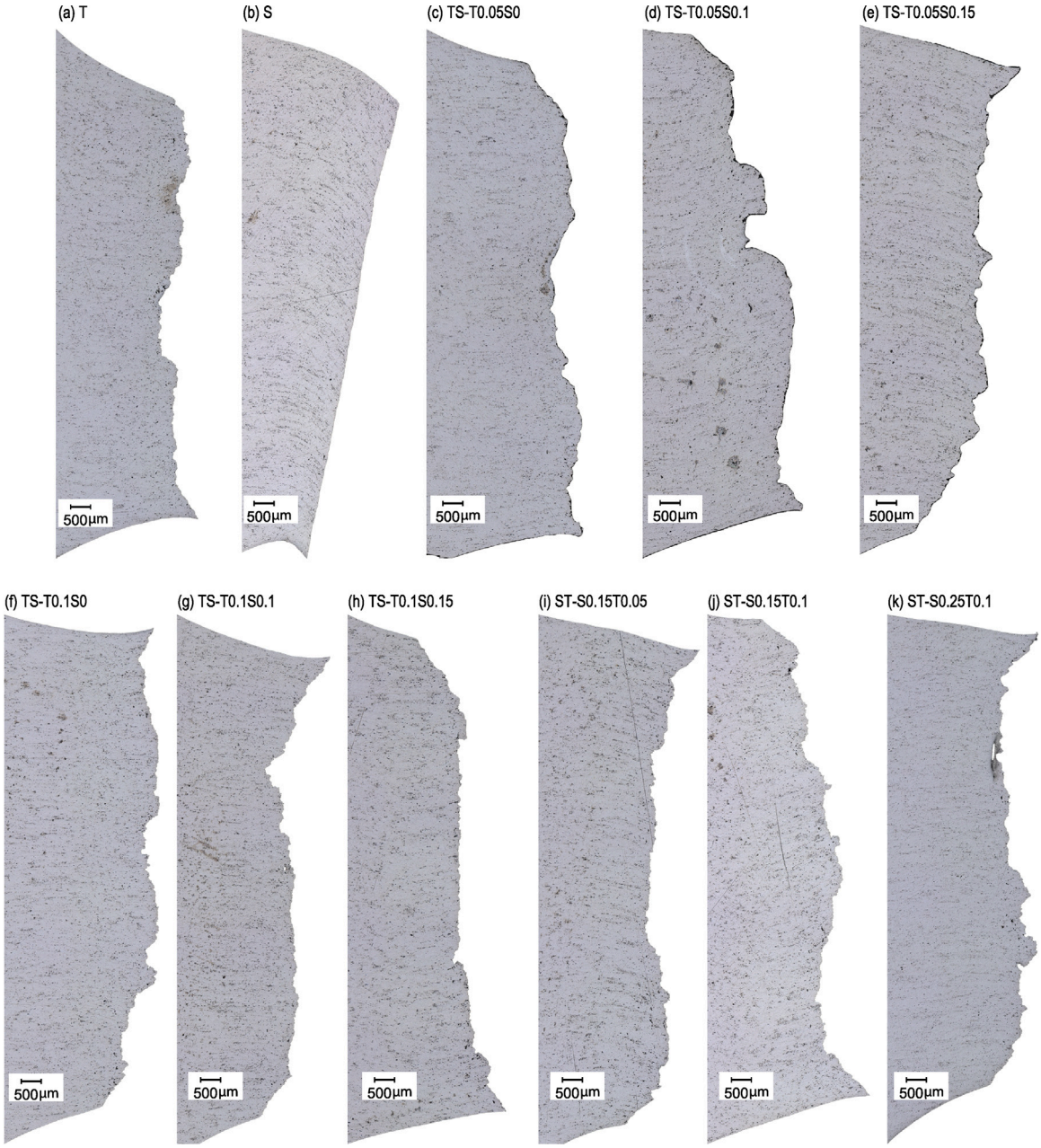

Fig. 17. Cropped light optical microscope (LOM) images of the fracture edges, taken from the edge regions near the fracture line.

damage strain, a consistent trend is also reflected in the SEM image analysis: both the void fraction and the mean size of micro-voids are smaller for loading patterns associated with lower fracture tensile displacements. For example, cyc-TS-T0.05S0.1 exhibits larger values than cyc-TS-T0.1S0.1, whereas cyc-TS-T0.05S0.15 results in smaller values than cyc-TS-T0.1S0.15. It is confirmed that different combinations of displacement increments in the respective tensile or shear directions during non-proportional loading histories lead to different onset and evolution of ductile damage. In addition, the mean void size under shear-to-tension (ST) loading is greater than that under tension-to-shear (TS) loading, even with the same displacement increment but different loading sequence. Similar to ST loading, different combinations of displacement increments in TS loading also lead to different material behavior at both global and local levels. These findings clearly reveal the influence of non-proportional loading history, loading sequence, and amplitude combinations on ductile damage behavior.

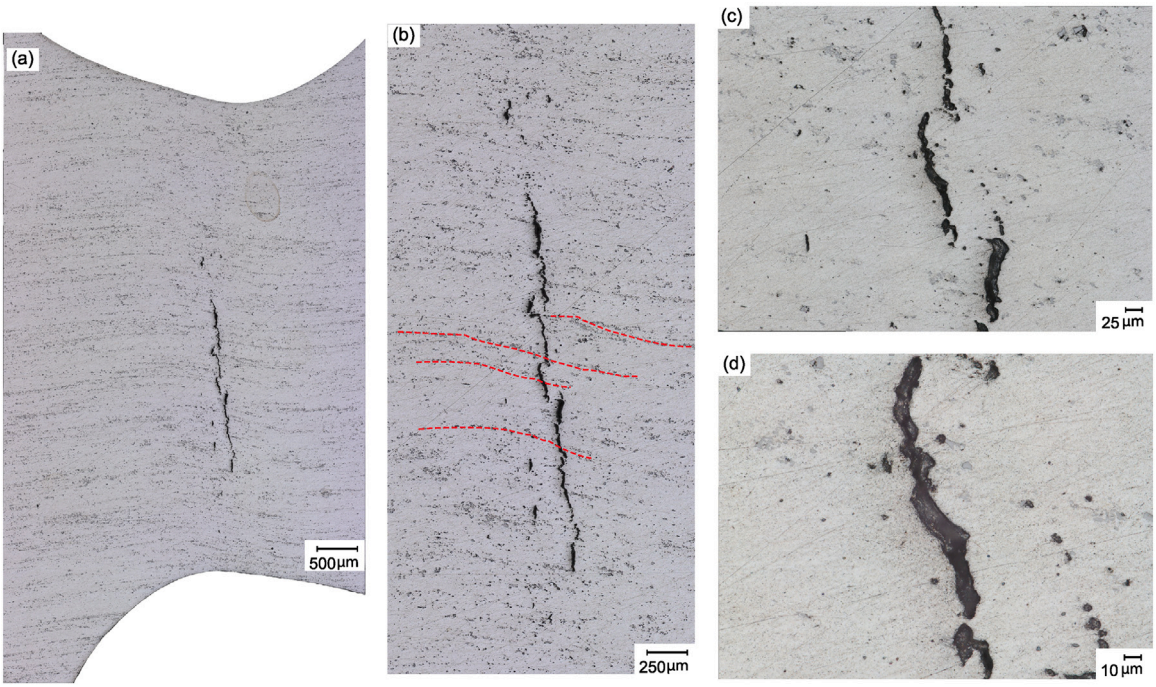

Fig. 18. Light optical microscope (LOM) images for the experiment cyc-TS-T0.05S0.1. (For interpretation of the references to color in this figure legend, the reader is referred to the web version of this article.)

CRediT authorship contribution statement

Zhichao Wei: Writing – original draft, Visualization, Software, Methodology, Investigation, Formal analysis, Data curation, Conceptualization. **Guoxi Mao:** Writing – review & editing, Validation, Investigation, Data curation. **Steffen Gerke:** Writing – review & editing, Validation, Methodology, Investigation, Conceptualization. **Sebastian Münstermann:** Writing – review & editing, Methodology, Investigation, Conceptualization. **Michael Brünig:** Writing – review & editing, Supervision, Resources, Project administration, Methodology, Funding acquisition, Conceptualization.

Declaration of competing interest

The authors declare that they have no known competing financial interests or personal relationships that could have appeared to influence the work reported in this paper.

Acknowledgments

The project has been funded by the Deutsche Forschungsgemeinschaft, Germany (DFG, German Research Foundation) – project number 322157331, this financial support is gratefully acknowledged. The SEM images of the fracture surfaces presented in this paper were performed at the Institut für Werkstoffe im Bauwesen, University of the Bundeswehr Munich and the support of Wolfgang Saur is gratefully acknowledged. All authors also thank student research associate Yijia Mo from the Institute of Metal Forming, RWTH Aachen University, for providing assistance in analyzing the SEM images using a machine learning approach and for valuable discussions. Zhichao Wei and Steffen Gerke also extend their congratulations to our co-author, Prof. Dr. Michael Brünig, on the occasion of his 65th birthday. We sincerely appreciate his outstanding contributions to the experimental and numerical analysis of ductile damage behavior.

Appendix A. Kinematic framework

To better understand the kinematic framework proposed by Brünig (2003), the configurations and associated metric transformations are illustrated in Fig. A.19. $\mathring{\mathcal{B}}$ denotes the reference configuration in the damaged configuration, while $\bar{\mathcal{B}}$ and $\mathcal{B}$ represent the current configurations within the damaged state. Similarly, $\mathring{\mathcal{E}}$ denotes the reference configuration in the effective fictitious undamaged configuration, and $\mathring{\mathcal{E}}$ and $\mathcal{E}$ represent the corresponding current configurations in this fictitious undamaged state.

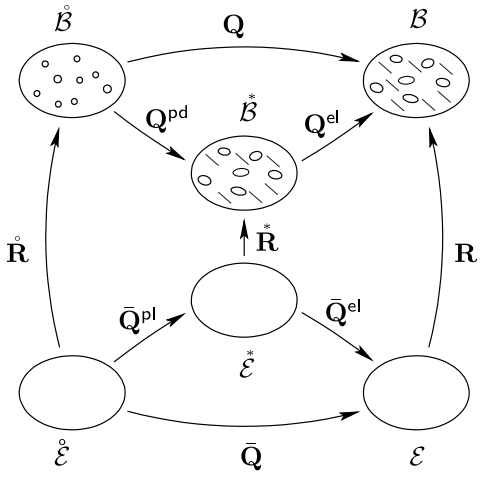

Fig. A.19. Configurations and metric transformation tensors (Brünig, 2003; Wei et al., 2024b). This figure has been previously published in Wei et al. (2024b), and is reproduced here under the terms of the Open Access license CC BY 4.0.

In the effective fictitious undamaged configurations ($\mathring{\mathcal{E}}$, $\overset{*}{\mathcal{E}}$, and $\mathcal{E}$), only the elastic–plastic behavior is considered, i.e., without accounting for damage effects. As shown in Fig. A.19, the kinematics between the reference and current effective fictitious undamaged configurations are described by the effective metric transformation tensor $\bar{\mathbf{Q}}$. Following Brünig (2003), it can be multiplicatively decomposed into an effective plastic part $\bar{\mathbf{Q}}^{\mathrm{pl}}$ and an elastic part $\bar{\mathbf{Q}}^{\mathrm{el}}$ as

$$\bar{\mathbf{Q}} = \bar{\mathbf{Q}}^{\mathrm{pl}}\bar{\mathbf{Q}}^{\mathrm{el}}\,. \tag{A.1}$$

In addition, the effective logarithmic strain tensor is defined as

$$\bar{\mathbf{A}} = \frac{1}{2}\ln\bar{\mathbf{Q}}\,, \tag{A.2}$$

and thus, the effective strain rate tensor is given by

$$\dot{\bar{\mathbf{H}}} = \frac{1}{2}\bar{\mathbf{Q}}^{-1}\dot{\bar{\mathbf{Q}}}\,. \tag{A.3}$$

Making use of Eq. (A.1), the effective strain rate tensor can be computed as

$$\dot{\bar{\mathbf{H}}} = \frac{1}{2}\bar{\mathbf{Q}}^{\mathrm{el}-1}\bar{\mathbf{Q}}^{\mathrm{pl}-1}\dot{\bar{\mathbf{Q}}}^{\mathrm{pl}}\bar{\mathbf{Q}}^{\mathrm{el}} + \frac{1}{2}\bar{\mathbf{Q}}^{\mathrm{el}-1}\dot{\bar{\mathbf{Q}}}^{\mathrm{el}} = \dot{\bar{\mathbf{H}}}^{\mathrm{pl}} + \dot{\bar{\mathbf{H}}}^{\mathrm{el}}\,, \tag{A.4}$$

where $\dot{\bar{\mathbf{H}}}^{\mathrm{el}}$ denotes the effective elastic strain rate tensor and $\dot{\bar{\mathbf{H}}}^{\mathrm{pl}}$ is the effective plastic strain rate tensor.

Compared to the effective fictitious undamaged configurations, the damaged configurations ($\mathcal{B}$, $\overset{*}{\mathcal{B}}$, and $\mathring{\mathcal{B}}$) additionally account for the effects of damage behavior induced by the evolution of micro-defects. The corresponding damage deformations can be determined by analyzing the relationship between the damaged and effective fictitious undamaged configurations, specifically through the initial damage tensor $\mathring{\mathbf{R}}$ and the current damage tensors $\mathbf{R}$ and $\overset{*}{\mathbf{R}}$, as illustrated in Fig. A.19. In addition, the logarithmic damage strain tensor is defined as

$$\mathbf{A}^{\mathrm{da}} = \frac{1}{2}\ln\overset{*}{\mathbf{R}}\,. \tag{A.5}$$

Following the multiplicative decomposition concept of the effective metric transformation tensor $\bar{\mathbf{Q}}$, the metric transformation tensor $\mathbf{Q}$ can also be expressed as

$$\mathbf{Q} = \mathbf{Q}^{\mathrm{pd}}\mathbf{Q}^{\mathrm{el}}\,, \tag{A.6}$$

where $\mathbf{Q}^{\mathrm{pd}}$ and $\mathbf{Q}^{\mathrm{el}}$ denote the plastic-damage and the elastic part of the metric transformation tensor, respectively.

Furthermore, the logarithmic strain tensor is defined as

$$\mathbf{A} = \frac{1}{2}\ln\mathbf{Q}\,, \tag{A.7}$$

thus, the total strain rate tensor is expressed as

$$\dot{\mathbf{H}} = \dot{\mathbf{H}}^{\mathrm{el}} + \mathbf{R}^{-1}\dot{\mathbf{H}}^{\mathrm{pl}}\mathbf{R} + \mathbf{Q}^{\mathrm{el}-1}\dot{\mathbf{H}}^{\mathrm{da}}\mathbf{Q}^{\mathrm{el}}\,, \tag{A.8}$$

where $\dot{\mathbf{H}}^{\mathrm{da}}$ describes the damage strain rate tensor modeling formation of inelastic strains caused by growth of micro-defects, see Brünig (2001, 2003) for more details.

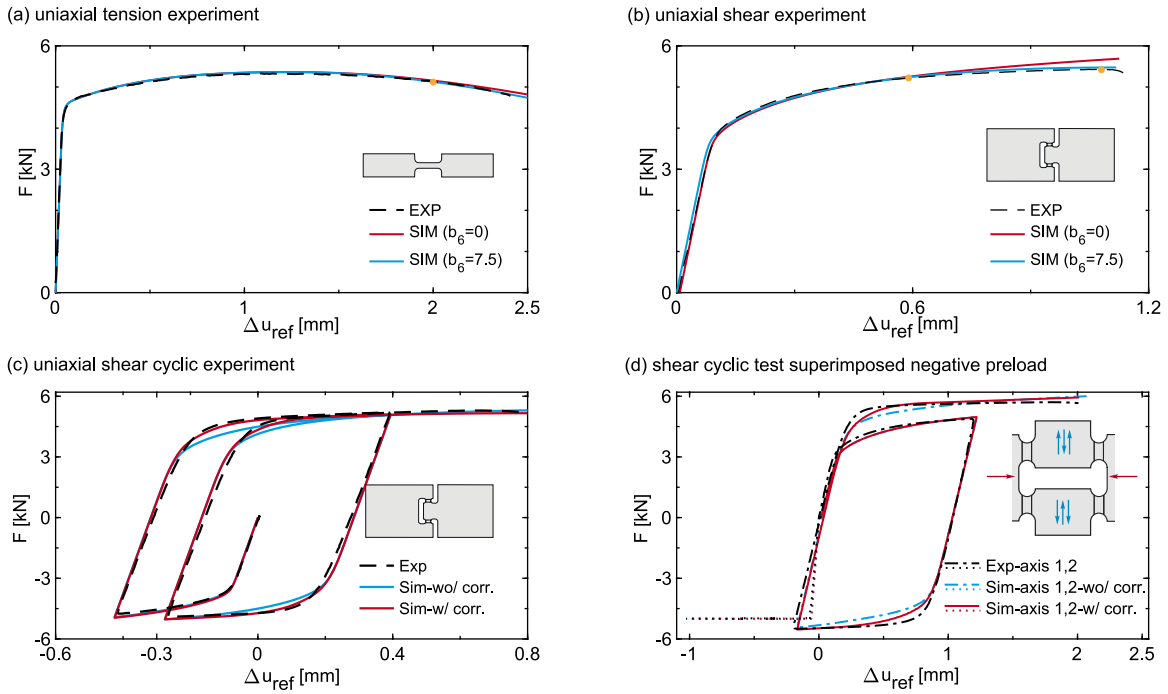

Fig. B.20. Experimental and numerical load–displacement curves for monotonic and cyclic experiments. The corresponding results are taken from (a) and (b) (Wei et al., 2025a), (c) (Wei et al., 2023a), and (d) (Wei et al., 2023b). It is worth mentioning that w/o corr. denotes without considering the change of hardening ratio after reverse loading, while w/ corr. denotes considering the change of hardening ratio after reverse loading (Wei et al., 2023b). Figs. (a)–(c) are reproduced under the terms of the CC BY 4.0 Open Access license.

Appendix B. Elastic, plastic and damage parameter identification

For proportional loading conditions, the proposed triple-term Voce strain hardening law in (19) can be simplified by omitting the third term and the effect of θ_b, which are associated with non-proportional loading. The simplified form is given by

$$\bar{c} = c_0 + Q_1(1 - e^{-p_1\gamma}) + Q_2\xi(1 - e^{-p_2\gamma})\,. \tag{B.1}$$

Similarly, the kinematic hardening law in (21) can be simplified as

$$\dot{\bar{\boldsymbol{\alpha}}}_1 = b_1\chi\dot{\mathbf{H}}^{\mathrm{pl}} - b_2\chi\dot{\gamma}\bar{\boldsymbol{\alpha}}_1\,, \quad \dot{\bar{\boldsymbol{\alpha}}}_2 = b_3\dot{\mathbf{H}}^{\mathrm{pl}} - b_4\dot{\gamma}\bar{\boldsymbol{\alpha}}_2\,, \quad \text{and} \quad \dot{\bar{\boldsymbol{\alpha}}}_3 = b_5\dot{\mathbf{H}}^{\mathrm{pl}} - b_6\dot{\gamma}\theta_a\bar{\boldsymbol{\alpha}}_3 \tag{B.2}$$

accordingly.

First, the force–displacement curves from the uniaxial tension and compression tests are converted into true stress–true strain curves without considering the onset of necking or buckling. These curves are then used to identify the basic elastic parameters (E, ν), the hydrostatic stress coefficient a/c in (4), and the plastic hardening parameters (c_0, Q_1, Q_2, p_1, p_2, $b_1 \ldots b_5$) in (B.1) and (B.2) by applying a least-squares fitting procedure to the measured uniaxial tensile stress–strain data. It should be noted that the parameter b_6 in the modified kinematic hardening law (B.2) mainly influences the material response under large plastic deformation due to the variation of θ_a. Therefore, in the initial step of the identification process, the influence of b_6 is neglected. Subsequently, b_6 is calibrated using an inverse fitting approach based on uniaxial tension and shear test results. The true stress–true strain curve from the tension–compression test is then used to identify the isotropic hardening ratio ρ_h in (23). Further details regarding the minimization functions and data processing can be found in Wei et al. (2025a, 2023b,a).

Compared with Fig. B.20(a) and (b), it is evident that introducing the nonlinear term in the third Chaboche kinematic hardening rule (B.2) is necessary. Although the model without this term ($b_6 = 0$) performs well for uniaxial tension experiments, it shows significant deviations from experimental results in the uniaxial shear test. In addition, Fig. B.20(c) and (d) compare simulations with and without considering the change in the hardening ratio after shear reverse loading. The results clearly demonstrate that the modification of the combined hardening law is essential. Further comparisons and discussions can be found in Wei et al. (2025a, 2023a,b).

The initial damage stress $\tilde{\sigma}_0$ (25) is identified using an inverse approach that combines experimental and numerical results. Based on a simulation that incorporates only the plasticity parameters, the true stress–true strain curve from the uniaxial tension test is compared with experimental data to determine the onset of damage. The stress-state-dependent parameters $\hat{\alpha}^{\mathrm{da}}$ and $\hat{\beta}^{\mathrm{da}}$ (8) in the damage condition (7), as well as $\tilde{\alpha}^{\mathrm{da}}$ (14) and $\tilde{\beta}^{\mathrm{da}}$ (15) in the damage strain rate tensor (13), are obtained from micro-simulations of

unit cells containing a micro-defect under different boundary conditions, generating a wide range of stress states. Through detailed analysis of the deformation and kinematic behavior within the unit cells, the relevant damage parameters are determined. These parameters are suitable for simulating a class of ductile metals without considering anisotropic plastic behavior, as mentioned in Brünig et al. (2013, 2016). Using this concept, Wei et al. (2023b) identified the softening parameters C_1 and C_2 in (25), and d_1 and d_2 in (26).

With the elastic, plastic, and damage parameters already identified, the newly introduced parameters related to hardening under non-proportional loading are calibrated. As discussed in Section 4, these parameters are inversely identified using experimental data from monotonic non-proportional loading tests reported by Brünig et al. (2021), as well as from the cyclic tests cyc-TS-T0.05S0.1 and cyc-ST-S0.25T0.1. Figs. 9 and 10 clearly demonstrate the accuracy of the proposed model in comparison with the experimental data. In addition, Fig. 8 shows that the newly introduced hardening behavior does not change the response under proportional loading conditions.

In addition, the current model does not account for distortional hardening resulting from changes in the yield surface shape under complex non-proportional loading, as noted in the introduction. A possible extension would be to introduce a stress-path-based kinematic hardening law, as proposed by Phillips and Weng (1975), which would only require adding an extra term to the current kinematic hardening law.

Appendix C. Previously designed biaxial experiments

The experimental and numerical load–displacement curves for different biaxial monotonic and cyclic loading experiments are shown in Figs. C.21, C.22 and C.23. All experimental data were obtained using the same aluminum alloy AW 6082-T6 as in this study, with the corresponding microstructure shown in Fig. 1. It is worth noting that all the numerical simulations use the same material parameters as listed in Table 3.

Fig. C.21(a)–(c) illustrate that the load is first applied along one of the biaxial axes until a predefined target and then kept constant while loading is superimposed on the other axis. This results in different tension–shear and compression–shear combinations, resulting in multiaxial stress states. Further details are provided in Wei et al. (2023b).

Fig. C.21(d) illustrates a single-cycle experiment, where a compressive load is first applied along the horizontal axis (indicated by the red arrow) until the predefined target force (e.g., −5 kN) is reached. The load is then held constant, and cyclic shear loading is subsequently applied along the vertical axis, as depicted by the blue arrow. It is worth noting that all cyclic loading cases are limited to up to 1.5 loading cycles. Details of the experimental setup and numerical results for different tensile and compressive loading conditions can be found in Wei et al. (2023b).

Fig. C.21(e) illustrates a biaxial bi-cyclic loading case with identical loading patterns applied along both axes, following a tension–compression–tension (TCT) sequence, as schematically indicated by the red and blue arrows. To investigate the influence of loading sequence on the material behavior, different combinations of loading sequences were performed. Due to the biaxial cyclic loading condition, a zero-strain-state can be achieved. However, the stress state only alternates between positive and negative values, without involving a tension–shear non-proportional loading path. Furthermore, all cyclic loading is limited to 1.5 cycles. The details of the experimental and numerical contributions can be found Fig. C.22.

Compared to previous studies, the number of loading cycles is increased, and different loading patterns are employed to investigate the effect of shear cyclic loading with varying loading amplitudes. It should be noted that the loading amplitudes are sufficiently large to induce ductile damage. As shown in Fig. C.21(f), cyclic loading with alternating positive and negative values is applied to the X0-specimen, resulting in a near-zero mean stress state, as illustrated by the red and blue arrows. For more details on the influence of different loading amplitudes, please refer to Wei et al. (2025b). The experimental and numerical results with different loading amplitudes are reproduced in Fig. C.23.

Appendix D. Experimentally measured force–time and displacement–time data

The experimental data will be made available upon request. The measured force–time plots for different cyclic loading conditions are shown in Fig. D.24, while the corresponding relative displacement–time plots are additionally presented in Fig. D.25. It should be noted that the machine displacement is not linearly correlated with the relative displacement between the gauge points, as defined by the measurement setup illustrated in Fig. 2(e).

Data availability

Data will be made available on request.

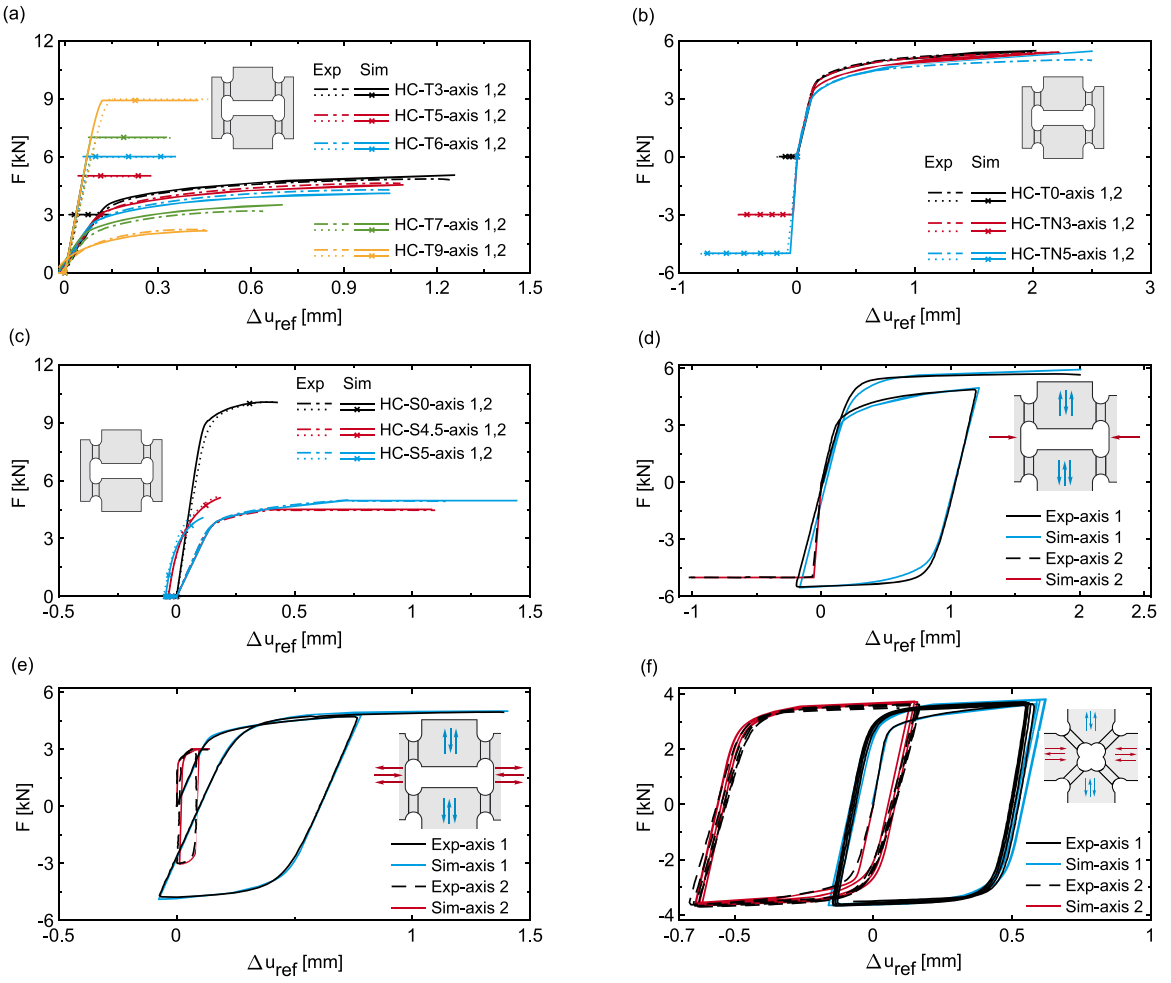

Fig. C.21. Experimental and numerical load–displacement curves for different biaxial monotonic and cyclic experiments: (a, b) tension/compression preload superimposed on shear load (Wei et al., 2023b); (c) shear preload superimposed on tension load (Wei et al., 2024b); (d) shear cyclic test superimposed on compressive preload (Wei et al., 2023b); (e) bi-cyclic experiment (Wei et al., 2024a); and (f) biaxially loaded shear cyclic experiment (Wei et al., 2025b). It is worth noting that T0–T9 in the subfigure denote tensile preloads, TN3–TN5 denote compressive preloads, and S0–S5 denote shear preloads, with the numbers indicating the magnitude. (For interpretation of the references to color in this figure legend, the reader is referred to the web version of this article.)

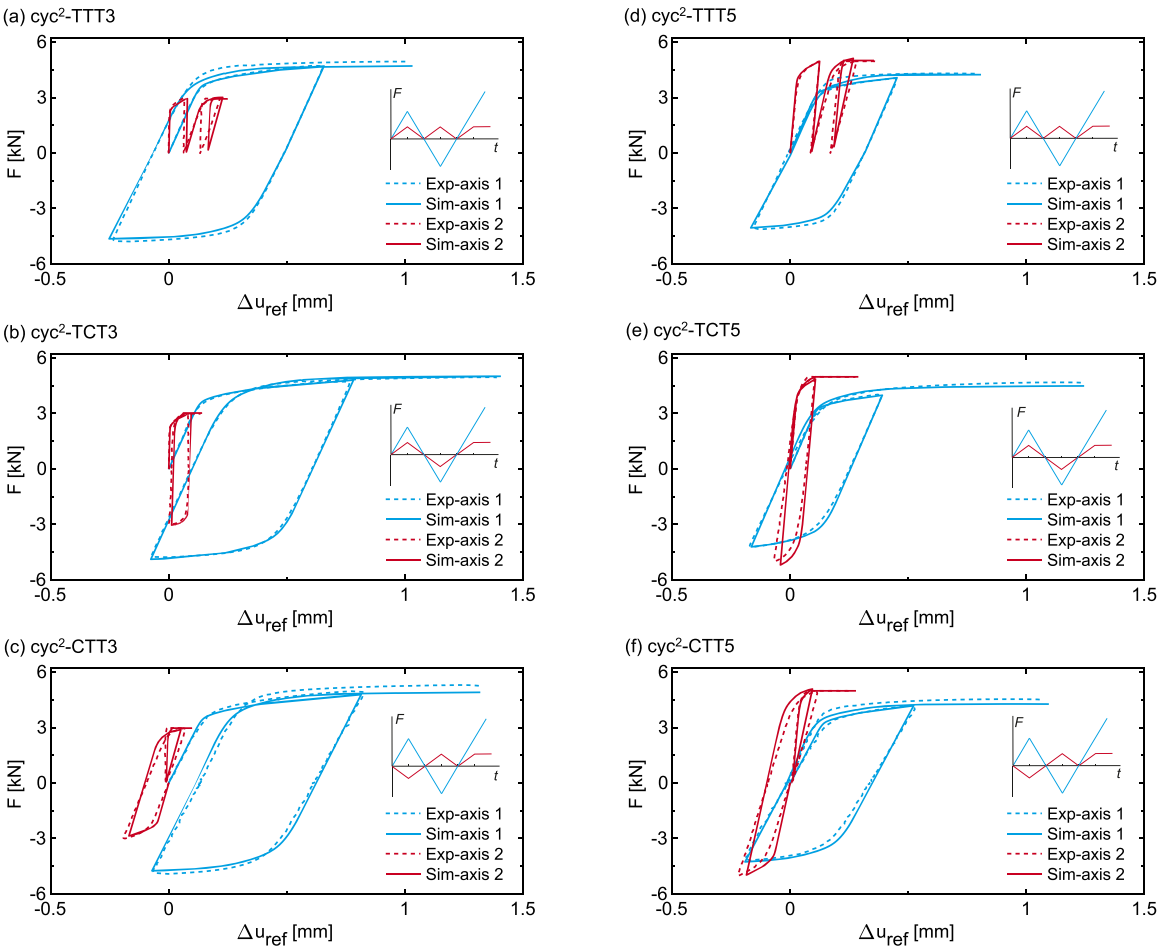

Fig. C.22. Experimental and numerical load–displacement curves for different bi-cyclic experiments. This figure has been previously published in Wei et al. (2024a), and is reproduced here under the terms of the Open Access license CC BY 4.0.

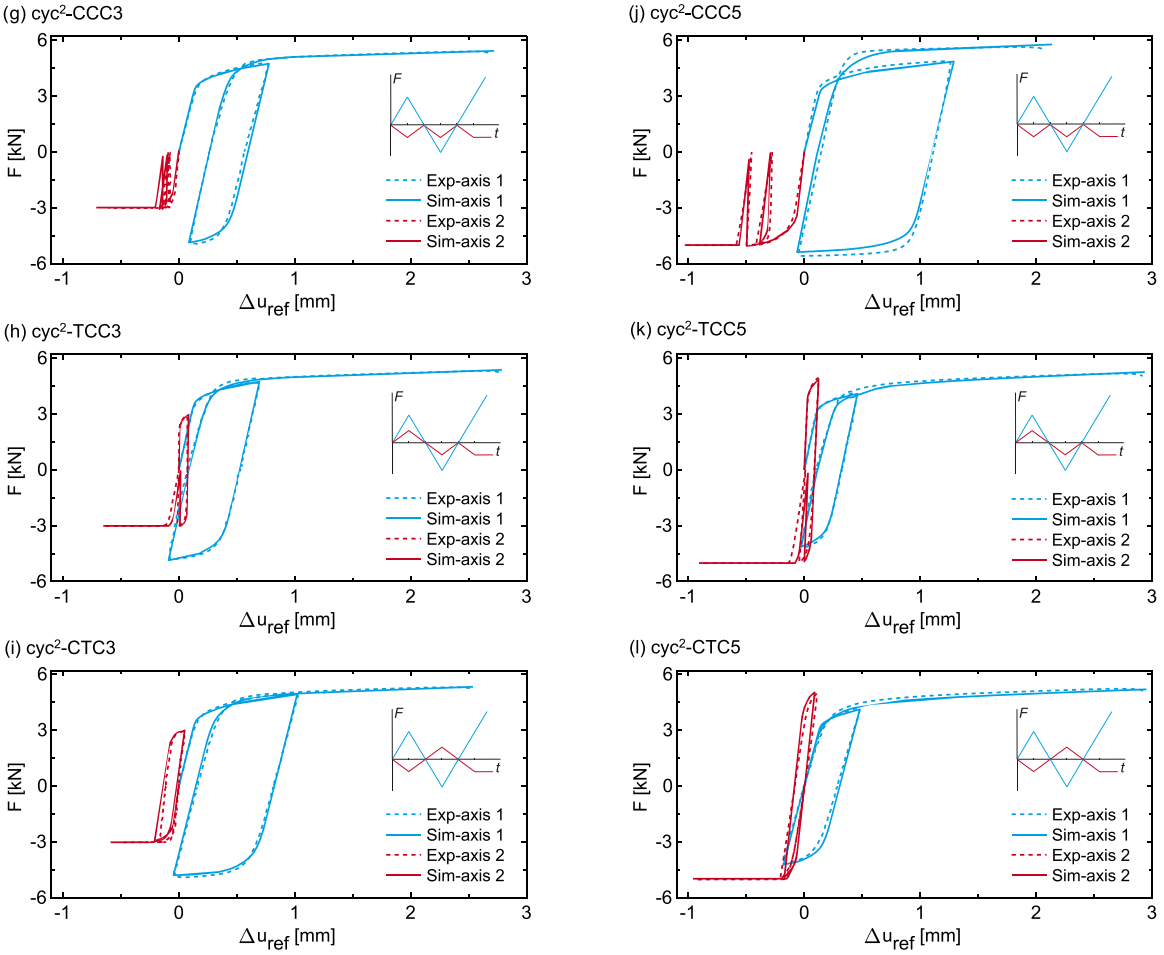

Fig. C.22. (*continued*).

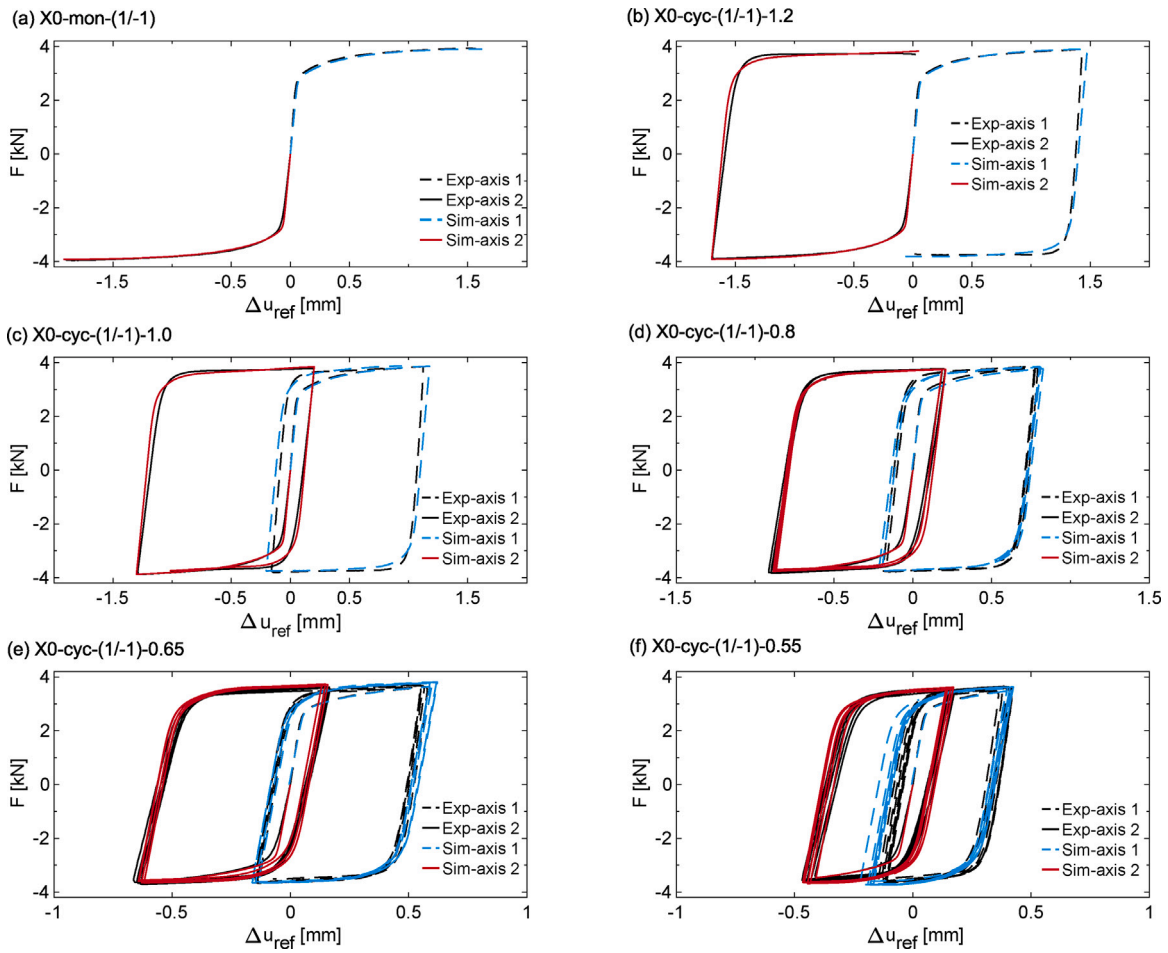

Fig. C.23. Experimental and numerical load–displacement curves for different biaxially loaded shear cyclic experiments. This figure has been previously published in Wei et al. (2025b), and is reproduced here under the terms of the Open Access license CC BY 4.0.

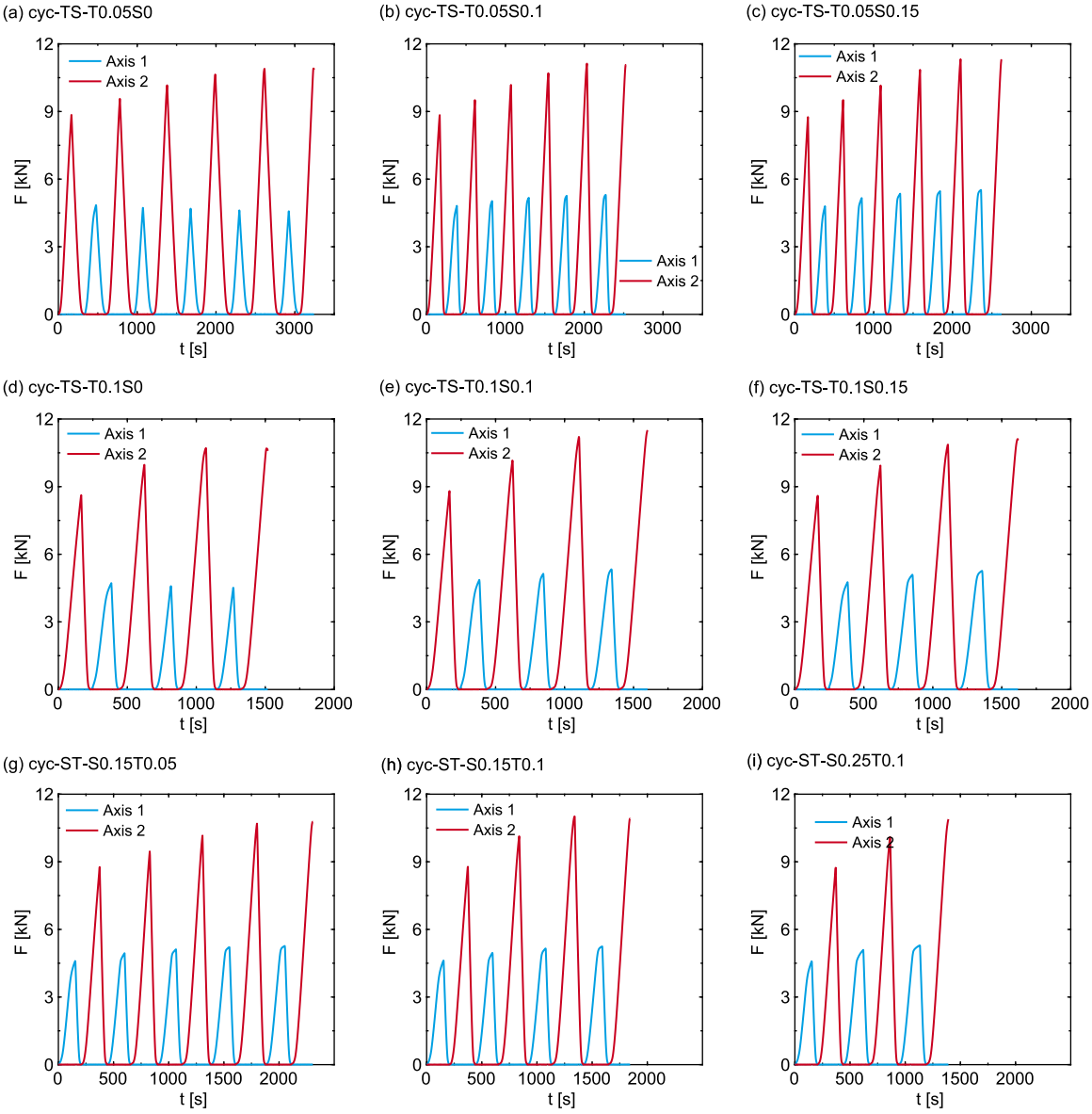

Fig. D.24. Experimentally measured force–time curves for the different designed cyclic loading patterns.

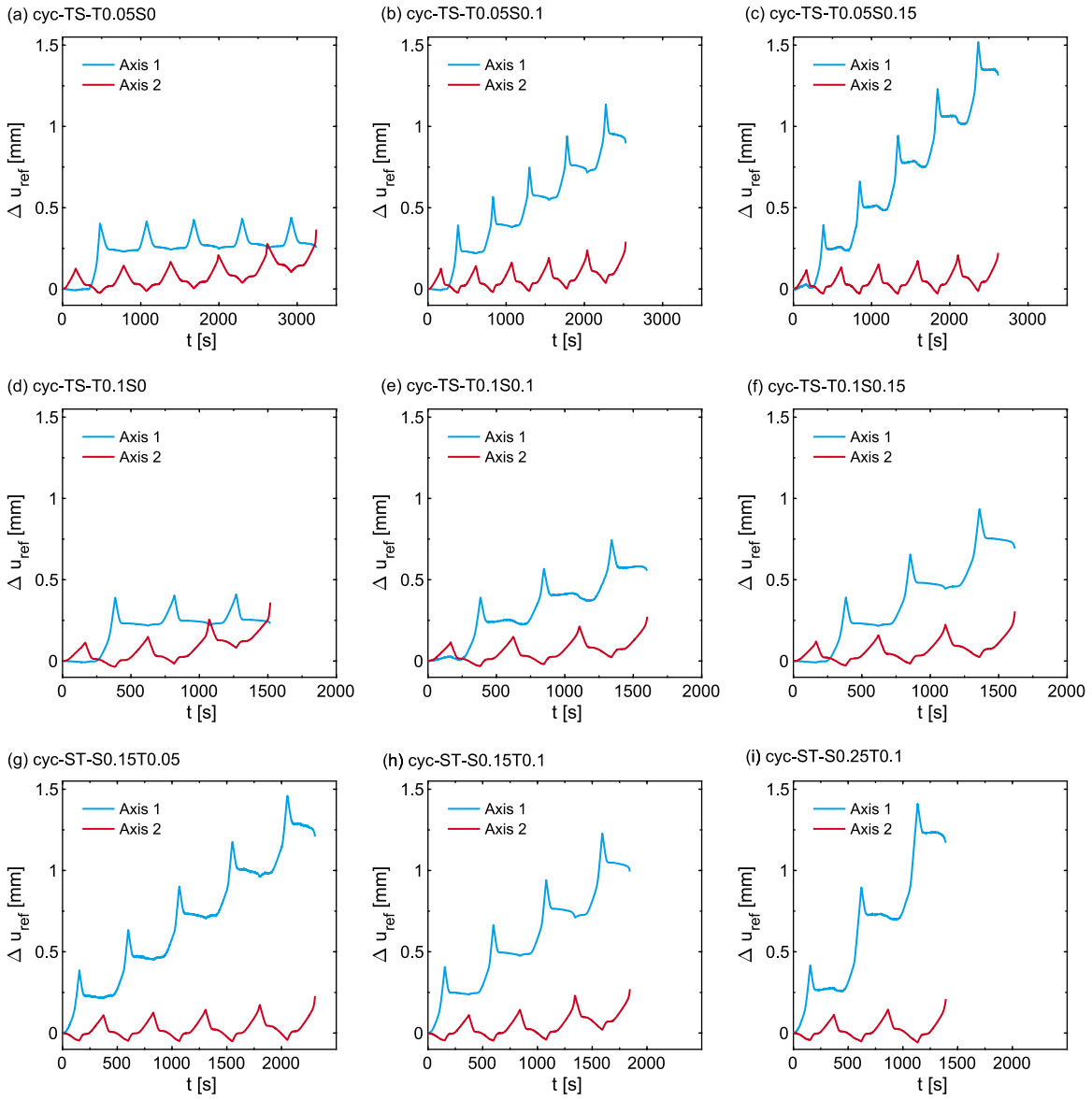

Fig. D.25. Experimentally measured relative displacement–time curves between the gauge points (see Fig. 2(e)) are presented for the different designed cyclic loading patterns.

References

Abu Al-Rub, R.K., Voyiadjis, G.Z., 2003. On the coupling of anisotropic damage and plasticity models for ductile materials. Int. J. Solids Struct. 40, 2611–2643.
Ansari, S., 2023. Building Computer Vision Applications using Artificial Neural Networks. A Press.
Badreddine, H., Saanouni, K., 2017. On the full coupling of plastic anisotropy and anisotropic ductile damage under finite strains. Int. J. Damage Mech. 26, 1080–1123.
Bai, Y., Wierzbicki, T., 2008. A new model of metal plasticity and fracture with pressure and Lode dependence. Int. J. Plast. 24, 1071–1096.
Balieu, R., Kringos, N., 2015. A new thermodynamical framework for finite strain multiplicative elastoplasticity coupled to anisotropic damage. Int. J. Plast. 70, 126–150.
Barlat, F., Gracio, J.J., Lee, M.G., Rauch, E.F., Vincze, G., 2011. An alternative to kinematic hardening in classical plasticity. Int. J. Plast. 27, 1309–1327.
Barlat, F., Yoon, S.Y., Lee, S.Y., Wi, M.S., Kim, J.H., 2020. Distortional plasticity framework with application to advanced high strength steel. Int. J. Solids Struct. 202, 947–962.
Benallal, A., Marquis, D., 1987. Constitutive equations for nonproportional cyclic elasto-viscoplasticity. J. Eng. Mater. Technol. 109, 326–336.
Brünig, M., 2001. A framework for large strain elastic–plastic damage mechanics based on metric transformations. Internat. J. Engrg. Sci. 39, 1033–1056.
Brünig, M., 2003. An anisotropic ductile damage model based on irreversible thermodynamics. Int. J. Plast. 19, 1679–1713.
Brünig, M., Chyra, O., Albrecht, D., Driemeier, L., Alves, M., 2008. A ductile damage criterion at various stress triaxialities. Int. J. Plast. 24, 1731–1755.

Brünig, M., Gerke, S., Hagenbrock, V., 2013. Micro-mechanical studies on the effect of the stress triaxiality and the Lode parameter on ductile damage. Int. J. Plast. 50, 49–65.
Brünig, M., Gerke, S., Schmidt, M., 2016. Biaxial experiments and phenomenological modeling of stress-state-dependent ductile damage and fracture. Int. J. Fract. 200, 63–76.
Brünig, M., Koirala, S., Gerke, S., 2023. A stress-state-dependent damage criterion for metals with plastic anisotropy. Int. J. Damage Mech. 32, 1811–1832.
Brünig, M., Zistl, M., Gerke, S., 2021. Numerical analysis of experiments on damage and fracture behavior of differently preloaded aluminum alloy specimens. Metals 11 (381).
Calloch, S., Marquis, D., 1999. Triaxial tension–compression tests for multiaxial cyclic plasticity. Int. J. Plast. 15, 521–549.
Chaboche, J.L., 1986. Time-independent constitutive theories for cyclic plasticity. Int. J. Plast. 2, 149–188.
Chaboche, J.L., 1988. Continuum damage mechanics: part I—general concepts. J. Appl. Mech. 55, 59–64.
Chen, K., Scales, M., Kyriakides, S., 2019. Material response, localization and failure of an aluminum alloy under combined shear and tension: Part II analysis. Int. J. Plast. 120, 361–379.
Cortese, L., Nalli, F., Rossi, M., 2016. A nonlinear model for ductile damage accumulation under multiaxial non-proportional loading conditions. Int. J. Plast. 85, 77–92.
Daroju, S., Kuwabara, T., Sharma, R., Fullwood, D.T., Miles, M.P., Knezevic, M., 2022. Experimental characterization and crystal plasticity modeling for predicting load reversals in AA6016-T4 and AA7021-T79. Int. J. Plast. 153, 103292.
Drucker, D.C., Prager, W., 1952. Soil mechanics and plastic analysis or limit design. Quart. Appl. Math. 10, 157–165.
Feigenbaum, H.P., Dafalias, Y.F., 2007. Directional distortional hardening in metal plasticity within thermodynamics. Int. J. Solids Struct. 44, 7526–7542.
François, M., 2001. A plasticity model with yield surface distortion for non proportional loading. Int. J. Plast. 17, 703–717.
Frederick, C.O., Armstrong, P.J., 2007. A mathematical representation of the multiaxial Bauschinger effect. Mater. High Temp. 24, 1–26.
Frodal, B.H., Dæhli, L.E.B., Børvik, T., Hopperstad, O.S., 2019. Modelling and simulation of ductile failure in textured aluminium alloys subjected to compression-tension loading. Int. J. Plast. 118, 36–69.
Gerke, S., Adulyasak, P., Brünig, M., 2017. New biaxially loaded specimens for the analysis of damage and fracture in sheet metals. Int. J. Solids Struct. 110-111, 209–218.
Gerke, S., Zistl, M., Bhardwaj, A., Brünig, M., 2019. Experiments with the X0-specimen on the effect of non-proportional loading paths on damage and fracture mechanisms in aluminum alloys. Int. J. Solids Struct. 163, 157–169.
Gerke, S., Zistl, M., Brünig, M., 2020. Experiments and numerical simulation of damage and fracture of the X0-specimen under non-proportional loading paths. Eng. Fract. Mech. 224, 106795.
Gurson, A.L., 1977. Continuum theory of ductile rupture by void nucleation and growth: part I—yield criteria and flow rules for porous ductile media. J. Eng. Mater. Technol. 99, 2–15.
Hou, Y., Lee, M.G., Lin, J., Min, J., 2022. Experimental characterization and modeling of complex anisotropic hardening in quenching and partitioning (Q & P) steel subject to biaxial non-proportional loadings. Int. J. Plast. 156, 103347.
Hou, Y., Myung, D., Park, J.K., Min, J., Lee, H.R., El-Aty, A.A., Lee, M.G., 2023. A review of characterization and modelling approaches for sheet metal forming of lightweight metallic materials. Mater. 16 (836).
Iftikhar, C.M.A., Khan, A.S., 2021. The evolution of yield loci with finite plastic deformation along proportional and non-proportional loading paths in an annealed extruded AZ31 magnesium alloy. Int. J. Plast. 143, 103007.
Jiang, Y., Kurath, P., 1997. Nonproportional cyclic deformation: critical experiments and analytical modeling. Int. J. Plast. 13, 743–763.
Jones, E., Iadicola, M., 2018. A good practices guide for digital image correlation. Int. Digit. Image Correl. Soc. 10, 1–110.
Kachanov, L.M., 1958. On rupture time under condition of creep. Otd. Techn. Nauk. 8, 26–31.
Kang, G., Li, Y., Gao, Q., 2005. Non-proportionally multiaxial ratcheting of cyclic hardening materials at elevated temperatures: Experiments and simulations. Mech. Mater. 37, 1101–1118.
Kanvinde, A.M., Deierlein, G.G., 2007. Cyclic void growth model to assess ductile fracture initiation in structural steels due to ultra low cycle fatigue. J. Eng. Mech. 133, 701–712.
Kong, X., Morgeneyer, T.F., Missoum-Benziane, D., Rousselier, G., 2023. A polycrystalline damage model applied to an anisotropic aluminum alloy 2198 under non-proportional load path changes. Int. J. Plast. 168, 103674.
Kurtyka, T., Życzkowski, M., 1996. Evolution equations for distortional plastic hardening. Int. J. Plast. 12, 191–213.
Lamba, H.S., Sidebottom, O.M., 1978. Cyclic plasticity for nonproportional paths: Part 1—cyclic hardening, erasure of memory, and subsequent strain hardening experiments. J. Eng. Mater. Technol. 100, 96–103.
Lemaitre, J., 1985. A continuous damage mechanics model for ductile fracture. J. Eng. Mater. Technol. 107, 83–89.
Li, H., Hu, X., Yang, H., Li, L., 2016. Anisotropic and asymmetrical yielding and its distorted evolution: Modeling and applications. Int. J. Plast. 82, 127–158.
Lian, J., Sharaf, M., Archie, F., Münstermann, S., 2013. A hybrid approach for modelling of plasticity and failure behaviour of advanced high-strength steel sheets. Int. J. Damage Mech. 22, 188–218.
Liu, F., Fu, Q., Chen, C., Liang, N., 2011. An elasto-plastic damage constitutive theory and its prediction of evolution of subsequent yield surfaces and elastic constants. Int. J. Plast. 27, 1355–1383.
Lou, Y., Yoon, J.W., 2023. Lode-dependent anisotropic-asymmetric yield function for isotropic and anisotropic hardening of pressure-insensitive materials. Part I: Quadratic function under non-associated flow rule. Int. J. Plast. 166, 103647.
Lou, Y., Zhang, S., Yoon, J.W., 2020. Strength modeling of sheet metals from shear to plane strain tension. Int. J. Plast. 134, 102813.
Marcadet, S.J., Mohr, D., 2015. Effect of compression–tension loading reversal on the strain to fracture of dual phase steel sheets. Int. J. Plast. 72, 21–43.
Min, J., Kong, J., Hou, Y., Liu, Z., Lin, J., 2022. Application of laser deposition to mechanical characterization of advanced high strength steels subject to non-proportional loading. Exp. Mech. 62, 685–700.
Ning, Z., Lv, X., Shi, S., Guo, X., Wang, S., Xu, B., Chen, G., 2025. A kinematic hardening constitutive model for anomalous multiaxial ratcheting behaviors of zirconium alloy tubes under combined cyclic axial load and internal pressure at 648 K. Int. J. Plast. 184, 104202.
Ohno, N., 1982. A constitutive model of cyclic plasticity with a nonhardening strain region. J. Appl. Mech. 49, 721–727.
Ohno, N., Nakamoto, H., Morimatsu, Y., Okumura, D., 2021. Modeling of cyclic hardening and evaluation of plastic strain range in the presence of pre-loading and ratcheting. Int. J. Plast. 145, 103074.
Otsu, N., 1979. A threshold selection method from gray-level histograms. IEEE Trans. Syst. Man Cybern. 9, 62–66.
Papasidero, J., Doquet, V., Mohr, D., 2015. Ductile fracture of aluminum 2024-T351 under proportional and non-proportional multi-axial loading: Bao–Wierzbicki results revisited. Int. J. Solids Struct. 69-70, 459–474.
Phillips, A., Weng, G.J., 1975. An analytical study of an experimentally verified hardening law. J. Appl. Mech. 42 (375).
Raj, A., Verma, R.K., Singh, P.K., Shamshoddin, S., Biswas, P., Narasimhan, K., 2022. Experimental and numerical investigation of differential hardening of cold rolled steel sheet under non-proportional loading using biaxial tensile test. Int. J. Plast. 154, 103297.
Scales, M., Chen, K., Kyriakides, S., 2019. Material response, localization, and failure of an aluminum alloy under combined shear and tension: Part I experiments. Int. J. Plast. 120, 340–360.
Shamsaei, N., Fatemi, A., Socie, D.F., 2010. Multiaxial cyclic deformation and non-proportional hardening employing discriminating load paths. Int. J. Plast. 26, 1680–1701.

Shang, X., Zhang, H., Wang, L., Zhu, G., Cui, Z., Fu, M.W., Zeng, X., 2021. The effect of stress state and strain partition mode on the damage behavior of a Mg-Ca alloy. Int. J. Plast. 144, 103040.
Shutov, A.V., Ihlemann, J., 2012. A viscoplasticity model with an enhanced control of the yield surface distortion. Int. J. Plast. 39, 152–167.
Skibicki, D., Pejkowski, Ł., Karolczuk, A., Seyda, J., 2022. Verification of the Tanaka non-proportional isotropic cyclic hardening model under asynchronous loading. Int. J. Solids Struct. 254–255, 111896.
Song, D., Kang, G., Yu, C., Kan, Q., Zhang, C., 2017. Non-proportional multiaxial fatigue of super-elastic NiTi shape memory alloy micro-tubes: Damage evolution law and life-prediction model. Int. J. Mech. Sci. 131–132, 325–333.
Spitzig, W.A., Richmond, O., 1984. The effect of pressure on the flow stress of metals. Acta Metall. 32, 457–463.
Spitzig, W.A., Sober, R.J., Richmond, O., 1975. Pressure dependence of yielding and associated volume expansion in tempered martensite. Acta Metall. 23, 885–893.
Tanaka, E., 1994. A nonproportionality parameter and a cyclic viscoplastic constitutive model taking into account amplitude dependences and memory effects of isotropic hardening. Eur. J. Mech. A/Solids 13, 155–173.
Tomstad, A.J., Boåsen, M., Faleskog, J., Børvik, T., Hopperstad, O.S., 2023. On the influence of stress state on ductile fracture of two 6000-series aluminium alloys with different particle content. Int. J. Solids Struct. 269, 112149.
Tvergaard, V., Needleman, A., 1984. Analysis of the cup-cone fracture in a round tensile bar. Acta Metall. 32, 157–169.
von Mises, R., 1913. Mechanik der festen Körper im plastisch- deformablen Zustand. Nachrichten Von der Ges. der Wiss. Zu Gött. Math.-Phys. Kl. 1913, 582–592.
Voyiadjis, G.Z., Hoseini, S.H., Farrahi, G.H., 2013. A plasticity model for metals with dependency on all the stress invariants. J. Eng. Mater. Technol. 135, 011002.
Wei, Z., Gerke, S., Brünig, M., 2023a. Characterization of ductile damage and fracture behavior under shear reverse loading conditions. Proc. Appl. Math. Mech. 23 (3), e202300031.
Wei, Z., Gerke, S., Brünig, M., 2023b. Damage and fracture behavior under non-proportional biaxial reverse loading in ductile metals: Experiments and material modeling. Int. J. Plast. 171, 103774.
Wei, Z., Gerke, S., Brünig, M., 2023c. Mechanical responses of ductile aluminum alloy under biaxial non-proportional tensile reverse loading patterns. Metals 13 (1922).
Wei, Z., Gerke, S., Brünig, M., 2024a. Ductile damage and fracture characterizations in bi-cyclic biaxial experiments. Int. J. Mech. Sci. 276, 109380.
Wei, Z., Gerke, S., Brünig, M., 2024b. Numerical analysis of non-proportional biaxial reverse experiments with a two-surface anisotropic cyclic plasticity-damage approach. Comput. Methods Appl. Mech. Engrg. 419, 116630.
Wei, Z., Gerke, S., Brünig, M., 2025a. Novel uniaxial and biaxial reverse experiments for material parameter identification in an advanced anisotropic cyclic plastic-damage model. Mech. Mater. 205, 105294.
Wei, Z., Harting, M., Gerke, S., Brünig, M., 2025b. Ductile damage analysis under extreme low-cycle biaxial shear loadings: Experiments and simulations. Int. J. Solids Struct. 313, 113292.
Wei, Z., Zistl, M., Gerke, S., Brünig, M., 2022. Analysis of ductile damage and fracture under reverse loading. Int. J. Mech. Sci. 228, 107476.
Wu, H., 2018. An empirical non-proportional cyclic plasticity approach under multiaxial low-cycle fatigue loading. Int. J. Mech. Sci. 142–143, 66–73.
Wu, H., Zhang, C., Yang, H., Zhuang, X., Zhao, Z., 2024. Extended Gurson-Tvergaard-Needleman model considering damage behaviors under reverse loading. Int. J. Mech. Sci. 272, 109196.
Wu, H., Zhuang, X., Zhao, Z., 2022. Extended GTN model for predicting ductile fracture under a broad range of stress states. Int. J. Solids Struct. 239–240, 111452.
Xing, R., Yu, D., Shi, S., Chen, X., 2019. Cyclic deformation of 316L stainless steel and constitutive modeling under non-proportional variable loading path. Int. J. Plast. 120, 127–146.
Yang, Y.F., He, Z.R., Ma, J., Yang, H., Min, J.Y., Zang, S.L., Li, H., 2022. Evolving asymmetric and anisotropic hardening of CP-Ti sheets under monotonic and reverse loading: Characterization and modeling. Int. J. Plast. 159, 103445.
Yoon, J.W., Lou, Y., Yoon, J., Glazoff, M.V., 2014. Asymmetric yield function based on the stress invariants for pressure sensitive metals. Int. J. Plast. 56, 184–202.
Zeng, C., Fang, X., 2023. Specimen geometry design for plasticity and fracture characterization of sheet metal under high testing speed and various stress states. Thin-Walled Struct. 186, 110688.
Zeng, C., Fang, X., 2025. A new yield surface model considering non-uniform strain rate hardening behavior. Int. J. Mech. Sci. 301, 110504.
Zistl, M., Brünig, M., Gerke, S., 2022. Analysis of damage and fracture behavior in ductile metal sheets undergoing compression and shear preloading. Int. J. Mater. Form. 15 (59).